

CHAPTER 1

Basic Soft Matter for Plants

YOËL FORTERRE

Aix-Marseille University, CNRS, IUSTI, Marseille 13013, France

Email: yoel.forterre@univ-amu.fr

This chapter provides an overview of fluid and solid mechanical concepts applied to plants. The objective is to present the main physical mechanisms and laws needed to describe some important physiological processes in plants, such as water and solute transport, growth, rapid movements and the feedback between mechanical signals and biology. Emphasis is given on presenting the various laws in their simplest mathematical form (avoiding tensorial formulation as much as possible), discussing the scaling laws and orders of magnitude relevant to plants. Many of the physical and biological concepts introduced in the chapter will be studied in more detail in subsequent chapters.

1.1 Fluids

Plants manipulate and move water to perform almost all their physiological functions. Yet, there is no microscopic “water pump” in plants that would “actively” transport water molecules across cells, as there is for proteins or ions. Therefore, whether minute transmembrane flows or large bulk transport through trees, all water movement in plants occurs passively, according to the well-known principles of thermodynamics and fluid mechanics. In this section, we review those mechanisms and present the main physical laws of water transport in plants. Readers interested in a more comprehensive presentation of both the biological and physical contexts

Soft Matter Series No. 15

Soft Matter in Plants: From Biophysics to Biomimetics

Edited by Kaare H. Jensen and Yoël Forterre

© The Royal Society of Chemistry 2023

Published by the Royal Society of Chemistry, www.rsc.org

may wish to consult recent reviews on the topic, such as Stroock *et al.*¹⁵³ or Jensen *et al.*⁷⁵

1.1.1 Water Potential and Turgor Pressure

1.1.1.1 Some Definitions

In plant science, it is common to characterize the thermodynamic status of water using *water potential* Ψ , defined as the chemical potential of water relative to a reference state, per unit volume:^{35,85,110,112}

$$\Psi = \frac{\mu_w - \mu_w^0}{\nu_w}. \quad (1.1)$$

Here μ_w is the chemical potential of water, *i.e.* the Gibbs free energy per unit mole, μ_w^0 is the chemical potential of water in the reference state, chosen to be pure liquid at atmospheric pressure and at ambient temperature, and $\nu_w \approx 18 \text{ cm}^3 \text{ mol}^{-1}$ is the molar volume of liquid water. Using this definition, the water potential has the dimension of a pressure (unit Pa or J m^{-3}) and is null for pure water at 1 atmosphere. The water potential depends on the thermodynamic state of water, *i.e.* its solid, liquid or gaseous state, the presence of other molecular constituents interacting with the water and the possible presence of an external field such as gravity acting on the water. We provide below the main expressions of water potential useful for plants.

- For a diluted aqueous solution under gravity, as found in the vessels of the vascular system or in the large vacuoles of cells (Box 1.1), the water potential may be decomposed as:

$$\Psi_{\text{liq}} = \Psi_p + \Psi_{\text{os}} + \Psi_g = P - c\mathcal{R}T + \rho gz. \quad (1.2)$$

The first term $\Psi_p = P$ is the enthalpic or pressure contribution to the water potential[†], where P is defined as the total pressure of the solution minus the atmospheric pressure. When referring to the pressure inside plant cells, this pressure difference is usually called the *turgor pressure*. The second term $\Psi_{\text{os}} = -c\mathcal{R}T$ is the osmotic contribution corresponding to the free enthalpy of mixing of the solute in water, as given by the van't Hoff's law. Here c is the solute concentration (unit mol m^{-3}), $\mathcal{R} \approx 8.31 \text{ J K}^{-1} \text{ mol}^{-1}$ is the ideal gas constant and T is the absolute temperature (unit Kelvin), such that $\mathcal{R}T \approx 2500 \text{ J mol}^{-1}$ at ambient temperature. The opposite of the osmotic term $\Pi = -\Psi_{\text{os}} = c\mathcal{R}T$, thereafter called the osmotic pressure, is often used instead of Ψ_{os} . Finally the last term $\Psi_g = \rho gz$ is the contribution of the external gravity field, where $\rho \approx 10^3 \text{ kg m}^{-3}$ is the water density, $g \approx 9.8 \text{ m s}^{-2}$ is the intensity of gravity and z is the altitude above ground.

[†]The compressibility of water is ignored in this expression; see Chapter 4.

Box 1.1 Biological background.

Figure 1.1a shows a typical plant cell as described in a biology textbook.¹⁵⁵ It consists of a water pocket – the vacuole – which can represent up to 95% of its volume, and the cytoplasm, which contains the cytoskeleton and the organelles necessary for the functioning of the cell, such as the nucleus, the chloroplasts and the mitochondria. Plant cells have various sizes depending on the organism, the type of cell and the stage of development, ranging from a few microns for the stem cells of buds to several centimeters for the giant cells of some aquatic algae^{sss}. Like any cell, the plant cell is surrounded by a semi-permeable plasma membrane, whose pore size allows water molecules to pass freely but prevents the passage of large solute molecules.

The main structural difference between animal cells and plant cells is the existence, in the latter, of a stiff wall surrounding the plasma membrane^{***}. This wall, whose thickness is of the order of 0.1 to 1 μm , allows the plant cell to sustain a very high internal hydrostatic pressure of the order of several bars, called turgor pressure (Section 1.1.1.2). The cell wall of plants is made of cellulose microfibrils embedded in a matrix of polysaccharides and proteins (Figure 1.1b). The cellulose microfibrils – the stiffer element of the wall – are produced from a protein complex that crosses the cell membrane and runs like a cargo along the cortical microtubules located inside the cell (Figure 1.1b). As a result, the orientation of the microfibrils deposited in the wall corresponds to the orientation of the cortical microtubules. This may impart mechanical anisotropy to the cell wall if the microtubule arrangement is anisotropic (Section 1.2.2.1).

Water in plants is generally taken up at the root level in the soil and transported throughout the plant body to the organs and leaves, where most of the absorbed water evaporates (Section 1.1.4). In compact, non-vascular tissue, such as in roots for radial transport or in the shoot growth zone, water follows two main pathways (Figure 1.1c). The first pathway, called the apoplast pathway, corresponds to transport in the cell wall only, the apoplast being defined as the plant volume contained outside the plasma membrane of cells. This pathway avoids the high hydraulic resistance of the plasma membrane but has a very small volume: the volume of the apoplast in non-vascular tissues is only 1–10% of the total tissue volume. In addition, the apoplast pathway does not allow for osmotic control of flow, because the cell wall is not very selective for solutes. The second pathway is the cell-to-cell pathway and includes the symplast and the transmembrane pathways. The symplast is defined as the volume contained within the plasma membrane of cells, and is thus the dual of

^{sss}Green algae and land plants belong to the Plantae kingdom, or “green plants”, characterized by the existence of chloroplasts containing green chlorophyll.

^{***}Other examples of walled organisms are fungi, bacteria and archaea.

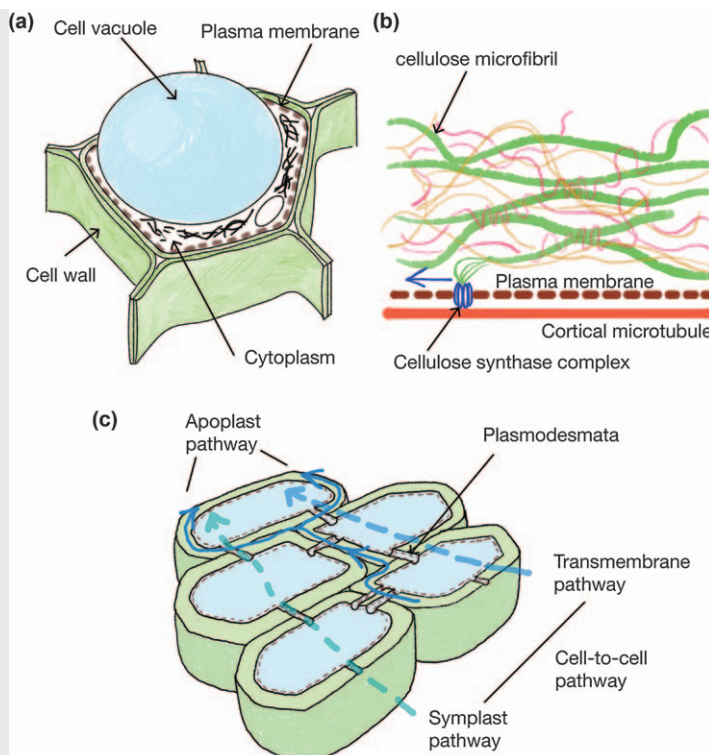


Figure 1.1 Basics of plant anatomy. (a) The plant cell. (b) The primary cell wall and the synthesis of the cellulose microfibrils, showing the cellulose microfibrils (green), hemicellulose (pink), pectin (beige), the plasma membrane (brown), the cellulose synthase complex (blue) and the cortical microtubule (orange). (c) Water pathways in non-vascular tissues. Drawings in (a) and (c) are inspired from the book.¹⁵⁵

the apoplast. It forms a continuous medium because the cytoplasms of the cells are connected to each other by plasmodesmata, small nanoscale pores whose permeability to water and solutes can be regulated⁶⁸ (see Chapter 2). The cell-to-cell pathway is under direct osmotic control by the cells.

As well as these pathways, most land plants have evolved specialized vascular tissues to carry water and other fluids over long distances. The xylem, on the one hand, is the pipe network that transports the sap, made of almost pure water, from the roots to the organs and leaves. It consists of long interconnected conduits made of dead cells typically 10 to 500 μm in width. Here transport is driven by a pressure gradient induced by evaporation and capillary cohesion in the leaves, which pulls water under negative pressures (Section 1.1.1.2 and Chapter 4). The phloem vascular network, on the other hand, is adjacent to the xylem and distributes the photosynthesis product created in the leaves (mainly sugar) to the rest of

the tissue for growth and storage. It consists of long living cells about 10 μm wide and 1 mm long separated by perforated sieve plates, forming a continuous symplastic pathway. Transport through the phloem is driven by an osmotic mechanism as explained in Section 1.1.3.2.

- The water potential of a humid vapor, as found inside leaves where gas exchange with the atmosphere takes place, is given by:

$$\Psi_{\text{vap}} = \frac{\mathcal{R}T}{\nu_w} \ln[\text{RH}] = \frac{\mathcal{R}T}{\nu_w} \ln\left(\frac{P_{\text{vap}}}{P_{\text{sat}}(T)}\right), \quad (1.3)$$

where $[\text{RH}] = P_{\text{vap}}/P_{\text{sat}}(T)$ is the relative humidity of the atmosphere, P_{vap} is the partial pressure of water in the vapor, $P_{\text{sat}}(T)$ is the saturation pressure of water in air[†] under atmospheric pressure and ambient temperature T ($P_{\text{sat}} = 2.3 \times 10^3$ Pa at 20 °C) and $\mathcal{R}T/\nu_w \approx 135$ MPa at 300 K[§].

- Finally, water is also found inside the cell wall of plants, where it binds with the cellulose network and other macromolecules such as hemicelluloses, pectins, and xyloglucans. The cell wall can be highly hydrated, as in the primary wall of growing cells, where about 75–80% of the wall volume is water,¹⁵⁵ or less hydrated, as in the lignified secondary wall of wood. The water potential of a gel-like medium akin to the cell wall is called the matrix (or matric) potential and denoted Ψ_m . The matrix potential of the cell wall depends on its water content, pH, temperature and the chemical affinity between the water molecules and the polymer constituents of the wall, mainly.¹¹² We provide in Box 1.4 an expression of the matrix potential for an ideal elastomeric hydrogel, derived from the theory of polymer solutions.

1.1.1.2 Consequences of Water Balance

At equilibrium, the chemical potential of water, and thus the water potential, must be uniform in all regions that can freely exchange water molecules. This basic thermodynamic statement has key consequences for the mechanical status of water in plants, which we briefly discuss below.

[†]The fact that the saturation pressure $P_{\text{sat}}(T)$ of water vapor *in air* appears in eqn (1.3), instead of the saturation pressure of a *pure* water vapor, comes from the choice of the reference state for the definition of the water potential (pure liquid under atmospheric pressure). In practice, these two definitions of the saturation pressure differ by less than 0.1%, so they are usually not distinguished (see the discussion in Chapter 4).

[§]The water potential of the vapor should include an additional gravity term $\Psi_g = \rho g z$, having the same expression as for a liquid phase. However, this contribution is usually negligible compared to the humidity term (eqn (1.3)).

First consider a plant cell containing solutes of concentration c immersed in an external bath of pure water at ambient atmosphere ($\Psi_{\text{bath}} = 0$) (Figure 1.2a). We assume that the cell is surrounded by an ideal semi-permeable membrane that allows water to pass freely through it but keeps solutes inside. Using eqn (1.2), equality of the water potential between the cell and the bath ($\Psi_{\text{cell}} = \Psi_{\text{bath}}$) implies that there exists a positive pressure difference, or turgor pressure, between the inside of the cell and the outside, given by $P = \Pi = cRT$. At equilibrium, the turgor pressure is thus equal to the osmotic pressure. For a solute concentration $c = 0.2 \text{ mol L}^{-1} = 200 \text{ mol m}^{-3}$, the turgor pressure is $P = 0.5 \text{ MPa}$. This is twice the pressure of a car tyre and larger than the typical tension $T_{\text{muscle}} \sim 0.2 \text{ MPa}$ produced by actin-myosin molecular motors and muscle-like fibers.¹³⁴ Such a large value of turgor

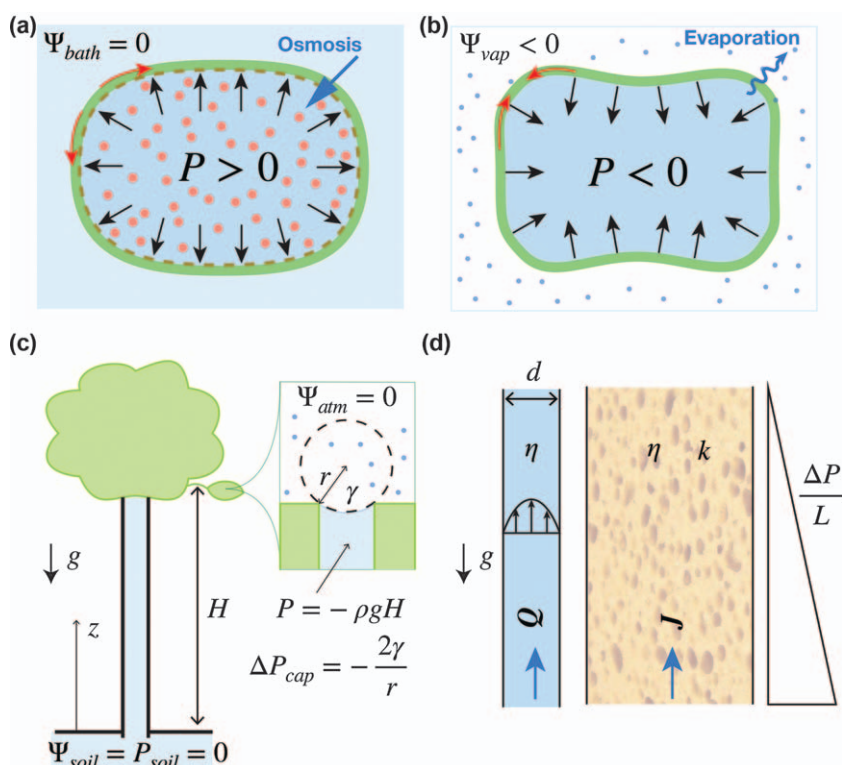


Figure 1.2 (a–c) Water potential balance and turgor pressure in plants. (a) Positive turgor pressure driven by osmosis for an isolated plant cell immersed in pure water (red arrows: tension in the cell wall). (b) Negative turgor pressure driven by evaporation for an isolated cell in equilibrium with a humid atmosphere (red arrows: compression in the cell wall). (c) The water column in the xylem of a tree is under tension (negative pressure). Mechanically, the column is held owing to a tiny capillary meniscus located at the cell wall/air interface (close-up sketch). (d) Pressure-driven flows: Poiseuille flow in a pipe (left) and Darcy flow in a porous medium of permeability k (right).

pressure is found routinely in hydrated plant cells, and can even reach up to 4 MPa – 40 bars! – in the stomata⁵⁵ or in the shoot apical meristem of *Arabidopsis*.⁹³ These high positive values of the turgor pressure can be achieved in plants because the cell is surrounded by a stiff cell wall (see Box 1.1). As we shall see in this chapter and throughout the book, turgor pressure plays a key role in plant biomechanics and physiology. It determines the rigidity of non-woody plant tissues and drives irreversible cell-wall deformation during growth. Change of turgor pressure driven by osmotic or evaporation gradients is also responsible for many reversible movements in plants.^{39,71}

The second application we consider is an evaporating cell in contact with a humid atmosphere at 1 bar (Figure 1.2b). If thermodynamic equilibrium is reached, equality of the water potential between the cell and the vapor ($\Psi_{\text{cell}} = \Psi_{\text{atm}}$) implies from eqn (1.2) and (1.3) a turgor pressure inside the cell given by $P = cRT + (RT/v_w)\ln[\text{RH}]$. For a 90% humidity, *i.e.* $[\text{RH}] = 0.9$, and a solution concentration $c = 0.2 \text{ mol L}^{-1}$ as before, the turgor pressure is $P = -14.5 \text{ MPa}$ or -145 bars ! In this situation, the turgor pressure is therefore highly negative, which means that the liquid water inside the cell is in tension and pulls on the cell wall. Large negative water pressures due to evaporation are indeed observed in plant cells with very rigid cell walls, such as in the woody cells of the xylem in trees. However, liquid water in tension is in a metastable state. If a gas germ of sufficient size nucleates or is already present inside the cell, cavitation may occur: the microscopic gas germ suddenly expands into a macroscopic bubble. The mechanism of bubble cavitation and its consequence for embolism formation in trees is discussed in Chapter 4. Negative water pressure, and more generally water tension in the cell wall of dead tissues, is also responsible for many passive movements in response to humidity change,^{19,76} such as the opening and closing of pine cones,³⁶ the bending of wheat awns⁴⁵ or the curling of seed pods.^{4,51} These hygroscopic movements are discussed in Chapter 7.

In the aforementioned examples, the change of water pressure is induced by osmotic or humidity gradients. We conclude by considering the more common situation of a pure water column in static equilibrium under gravity, as found in the vessels of a tall tree in the absence of flow (Figure 1.2c). At equilibrium, the water potential of the sap $P + \rho g z$ given by eqn (1.2) must be uniform along the column. Assuming that the water potential is zero, which corresponds to a well-watered soil, the water pressure at the top of the tree is negative and given by $P = -\rho g H \simeq -0.5 \text{ MPa}$ for a 50 meter-tall tree of height H . It is interesting to compute the size of the capillary meniscus needed to support this negative pressure difference mechanically. The Young–Laplace law states that the pressure difference ΔP_{cap} between water and air at a curved spherical interface is given by:

$$\Delta P_{\text{cap}} = -\frac{2\gamma}{r}, \quad (1.4)$$

where $\gamma \sim 0.07 \text{ N m}^{-1}$ is the surface tension of the water/air interface and r is the radius of curvature of the meniscus, counted positive if the meniscus is curved toward the air. For $\Delta P_{\text{cap}} \sim -\rho g H \sim -0.5 \text{ MPa}$, the radius of curvature of the meniscus is about $0.3 \text{ }\mu\text{m}$. This value is at least one order of magnitude smaller than the size of the smallest conductive vessels of the xylem found in leaves. Therefore, air/liquid capillary suction in the xylem cannot be the mechanism of sap ascent in trees. By contrast, the wall of plant cells is a hydrogel with nanometer-size pores that are small enough to support a very large mismatch of capillary pressure across the water/air interface (Figure 1.2c, close-up). Therefore, the negative water pressure in the vascular system of plants is mechanically balanced at the cell wall level, thanks to the reduction of the matrix water potential: $\Psi_{\text{m}} = -\rho g H$. This equilibrium of water under negative pressure holds only if there exists a continuous path of liquid from the ground to the leaves in contact with the atmosphere, where water eventually evaporates. The coupling between water in tension inside the xylem, capillary suction by the cell wall and evaporation at the cell wall/air interface is the basis of the cohesion-theory of sap ascent.³⁸ The reader interested in xylem flows can consult Tyree and Zimmermann's book¹⁶⁰ or recent reviews such as ref. 75 and 153.

In the previous examples we have considered situations of thermodynamic equilibrium, corresponding to a uniform water potential and no water flux. Water transport requires the presence of water potential gradients, which can arise from pressure gradients, solute concentration gradients, or humidity gradients. We now discuss the laws relating these gradients to water fluxes.

1.1.2 Pressure-driven Flows

1.1.2.1 Viscous Flows

Flows inside plants occur in tiny pipes. The largest conducting vessels in trees are barely larger than 0.1 mm in diameter (with a range of diameters from $10 \text{ }\mu\text{m}$ to $500 \text{ }\mu\text{m}$ ¹⁶⁰), while water pores inside the cell wall or the cell membrane are nanometric in size. Hence, although the pressure difference driving water transport in plants may be very large ($\sim\text{MPa}$ range), the viscous dissipation is huge, leading to small flow velocities. For example, the typical velocity U of the sap inside the xylem of trees during the day is a few meters per hour ($\sim 1 \text{ mm s}^{-1}$) for a vessel diameter $d \sim 100 \text{ }\mu\text{m}$.¹⁶⁰ The Reynolds number of this flow, which compares inertial to viscous effects, is:

$$\text{Re} = \frac{\rho U d}{\eta}, \quad (1.5)$$

where $\rho \simeq 10^3 \text{ kg m}^{-3}$ is the sap density and $\eta \simeq 10^{-3} \text{ Pa s}$ is the sap viscosity, giving a Reynolds number $\text{Re} \sim 0.1$ smaller than 1. Similarly, change of velocity usually occurs on timescales T from minutes to a day, which are much

Box 1.2 Methods for measuring the turgor pressure at cellular resolution.

Turgor pressure plays a central role in plant physiology and biomechanics. The development of accurate methods to measure turgor has thus always been a goal for plant scientists. Most methods give access, not directly to the turgor pressure P , but to the water potential Ψ or the osmotic pressure Π . If both quantities are known, then P is simply deduced from $P = \Psi + \Pi$. The main methods for measuring Ψ and Π are described, for example, in Taiz and Zeiger's book.¹⁵⁵ These include (i) plasmolysis, by bathing the cells in osmotic solutions of varying concentrations and determining the onset for plasmolysis, *i.e.* the bath concentration for which cell turgor drops to zero; (ii) the use of pressure chambers, or pressure bombs, which pressurize tissues until water is expelled, when the applied pressure is equal to the initial tissue water potential; (iii) psychrometers or cryoscopic osmometers, which deduce the osmotic pressure from its effect on the shift in some thermodynamic properties. Besides being indirect, these methods only give access to the global water status of the tissue, assuming the equilibrium of the water potentials. By contrast, the two techniques described below can be used to determine the turgor pressure at cellular resolution, without assuming thermodynamic equilibrium.

The first method, known as the pressure probe, consists in introducing a microcapillary directly inside the cell vacuole to record the pressure (Figure 1.3a). The first detailed measurements were made in 1967 by Green and Stanton on giant algal cells, using a capillary filled with air and closed at one end.⁶² The size of these cells (diameter of about 2 mm for a length of several centimeters) was large enough to neglect the loss of cell sap upon insertion of the capillary and to obtain the turgor pressure directly from the change of air volume in the capillary, using the ideal gas law $PV = nRT$. For smaller cells, however, this technique cannot be used, because the compressibility of the measuring system is too large compared to the compressibility of the cell. To overcome this difficulty, the cellular pressure probe was developed in the 1970s by Steudle and Zimmermann¹⁵⁰ (a detailed presentation of the method can be found in ref. 149). The tip of the capillary is reduced to a few microns and the capillary is filled with a liquid – silicone oil – and connected to a closed oil-filled chamber containing a pressure transducer and a piston. When the tip of the capillary is inserted into the cell, cell sap compresses the oil inside the capillary, forming a sap/oil meniscus near the tip that is visible under a microscope. At equilibrium, when the meniscus is maintained at a fixed position with the piston, the pressure measured in the chamber is equal to the turgor pressure inside the cell (the capillary pressure jump across the meniscus is usually negligible).

The pressure probe not only provides access to the turgor pressure, but also enables the measurement of the elastic and hydraulic properties of

the cell. For this purpose, a rapid increase of the cell volume ΔV is applied by means of the piston, after which the pressure relaxation is measured by keeping the meniscus position fixed (Figure 1.3a). The initial relationship between ΔV and ΔP gives access to the elastic bulk modulus of the cell: $B_{\text{cell}} = V(\Delta P/\Delta V)$, providing that the cell volume V is known (eqn (1.33) in Section 2.2). The relaxation timescale of the pressure, on the other hand, gives access to the cellular relaxation time $\tau_{\text{cell}} = V/[L_p S(B_{\text{cell}} + \pi)]$ discussed in Section 2.3 (eqn (1.39)), enabling measurements of the plasma membrane hydraulic permeability L_p . The cellular pressure probe has been used to determine water relations in various plant cells and organs, including negative pressure in the xylem.¹⁶⁵ Recently, a somewhat simplified version has been developed, the pico gauge,⁸² in which most of the volume of the capillary is filled with a resin that solidifies under UV light, the oil volume being reduced to the very tip of the capillary. As in Green's pioneering experiments, the pressure is deduced from the compression of the oil volume upon insertion into the cell, obtained from image analysis.

The cell pressure probe is unique in giving a direct measure of the cell turgor. However, this method is invasive and time-consuming and becomes increasingly difficult as the cell size decreases typically below 20 μm . This has motivated the development of alternative indentation-based methods in recent years.^{56,97,164} Lintilhac *et al.* in 2000 were the first to use indentation to access the turgor of onion epidermal cells, using beads in the range 50–500 μm in diameter (ball tonometry method⁹¹). The turgor was simply derived from the indentation contact area A measured optically and the indentation force F assuming $F = PA$. However, for smaller cells, probes or indentation depths, the determination of the contact area may be difficult. The influence of the wall tension and cell wall elasticity, ignored in their analysis, can also be important.

Recently, the use of atomic force microscopy (AFM) techniques with smaller probes (submicron in size) has made it possible to determine, from a single indentation curve, both the elastic properties of the wall and the cell turgor, providing that the cell topography is known¹¹ (Figure 1.3b). The Young's modulus of the wall is first determined from the small indentation-depth portion of the curve, for indentation δ much smaller than the cell wall thickness h , using the classical contact Hertz's law: $F \propto E_{\text{wall}} \sqrt{R_{\text{probe}}} \delta^{3/2}$. Interpreting the larger depth portion of the curve requires a model for the indentation of an inflated shell.¹⁶¹ Assuming the radius of the probe to be much smaller than the cell size and indentation not too large ($\delta \sim h$), a linear relationship is predicted between force and indentation: $F = k\delta$. The apparent stiffness k is a function of the cell topography (obtained with the AFM), the cell wall elasticity (determined previously) and the turgor pressure, from which P is obtained. When these assumptions are not fulfilled, disentangling turgor pressure and wall elasticity from the indentation curve is not obvious and mostly requires the use of finite element method (FEM) simulations.^{93,135}

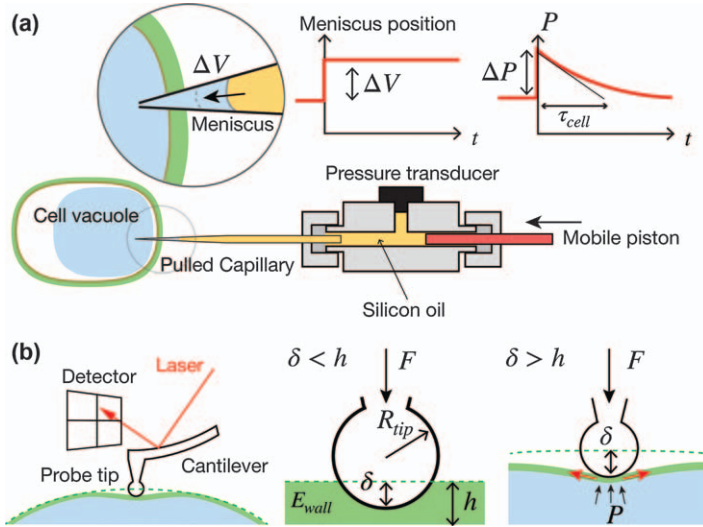


Figure 1.3 Measurements of the turgor pressure at cellular resolution. (a) Cellular pressure probe. (b) Nanoindentation (figure redrawn and adapted from ref. 93). Left: principle of the AFM technique. Center: small indentation depths δ give access to the cell wall elasticity. Right: large indentation depths are sensitive to both the local cell geometry, cell wall elasticity and turgor pressure.

longer than the timescale of momentum diffusion across the diameter of the pipe given by $\tau \sim \rho d^2 / \eta \sim 0.01$ s, such that the Stokes number, defined as:

$$St = \frac{\tau}{T} = \frac{\rho d^2}{\eta T} \quad (1.6)$$

is much smaller than 1.

Therefore, inertial effects can usually be ignored when dealing with water transport in plants. In this situation, the Navier–Stokes equation of fluid mechanics reduces to the Stokes equation, balancing the pressure gradient and the viscous stress:

$$-\nabla P + \eta \Delta \mathbf{U} + \rho \mathbf{g} = 0 \quad (1.7)$$

whereas mass conservation imposes that:

$$\nabla \cdot \mathbf{U} = 0 \quad (1.8)$$

where \mathbf{U} is the local velocity field of the flow and \mathbf{g} the gravity vector.

1.1.2.2 Hagen–Poiseuille’s Law

Integrating eqn (1.7) and (1.8) in the case of an infinitely long, vertical pipe of circular cross-section of diameter d , like the conducting vessels of the

xylem (Figure 1.2d), gives Hagen–Poiseuille’s law, relating the flow rate Q (unit $\text{m}^3 \text{s}^{-1}$) and the pressure gradients along the pipe:

$$Q = -\frac{\pi d^4}{128\eta} \nabla(P + \rho g z). \quad (1.9)$$

One recognizes a linear relationship between the flow rate (the “flux”) and the gradient of water potential (the “force”)[†]. The coefficient of proportionality defines the conductivity K of the pipe (conductance per unit length), which varies as the vessel diameter to the power 4. Hence, when the vessel diameter decreases in an ideal branch by N identical pipes in parallel, an increasing number of vessels $N \propto d^{-4}$ is needed to achieve the same flow rate under a given pressure gradient.

1.1.2.3 Darcy’s Law

The previous relationship can be generalized to pressure-driven flows in a continuum porous material (Darcy’s law):

$$\mathbf{J} = \frac{\kappa}{\eta} \nabla(P + \rho g z), \quad (1.10)$$

where \mathbf{J} is the flow rate per unit area (unit m s^{-1}) and κ (unit m^2) is the hydraulic permeability of the porous material (Figure 1.2d). The hydraulic permeability scales with the pore size d as $\kappa \propto d^2$ and may be anisotropic, like in the xylem where flow in the longitudinal direction along the vessels is much easier than in the transverse direction. Assuming an ideal tree branch made of N identical pipes of diameter d in parallel, it is possible to explicitly find the relationship between κ and d . The flow rate per unit area is $J = NQ/S$, where Q is the flow rate across a single pipe and S is the area of the cross-section of the branch. Using Hagen–Poiseuille’s law (eqn (1.9)) and identifying with Darcy’s law gives an effective longitudinal permeability for the branch $\kappa_{\text{xylem}} = (d^2/32)\phi_{\text{xylem}}$, where $\phi_{\text{xylem}} = N\pi(d^2/4)/S$ is the surface fraction of xylem. Typical order of magnitudes for $d \sim 10\text{--}100 \mu\text{m}$ and $\phi_{\text{xylem}} \sim 0.2$ give permeability values in the range $\kappa_{\text{xylem}} \sim 10^{-13}\text{--}10^{-11} \text{ m}^2$, similar to the permeability of fine granular soils (silt). By contrast, the hydraulic permeability of the cell wall is much lower, $\kappa_{\text{wall}} \simeq 10^{-17} \text{ m}^2$, which corresponds to water pores in the cellulosic matrix of nanometric size $d \sim 3\text{--}4 \text{ nm}$.^{20,49} For such an hydrogel made of microscopic pores, Darcy’s law can be generalized as $\mathbf{J} = -(\kappa/\eta)\nabla\Psi_{\text{wall}}$, with $\Psi_{\text{wall}} = \Psi_m + \rho g z$ (see Box 1.4).

[†]Note that the gradient of solute does not appear in this expression. Indeed, the diffusion of solute alone, without pressure gradient, is not associated with a global volume flux in the absence of semi-permeable membranes. This is because the volume flux of solute in this case is exactly compensated by an equal and opposite volume flux of water molecules, such that $Q = 0$ (this corresponds to a reflection coefficient $\sigma_S = 0$; see Section 1.1.3). This may not be the case if the solute interacts with an external field in very narrow channels, as in diffusio-phoresis and electro-osmosis.

1.1.3 Osmotic Flows and Solute Transport

Pressure-driven flows are very efficient in carrying water over long distances and are the main mode of water transport in the apoplast of plants (xylem, cell wall). Another important mode of transport in plants is osmosis, which occurs when solute concentration gradients exist across the semi-permeable membranes of living cells.

1.1.3.1 Water Transport Across Cell Membranes

The transport of water and solute across a semi-permeable membrane like the plasma membrane of cells can be described using the framework of irreversible thermodynamics and the linear response between “forces” and “flux” (Onsager relations).^{35,47,77,148} In the presence of a pressure difference ΔP and concentration difference Δc across the membrane, a volume flux (essentially water) J (unit m s^{-1}) and a molar flux of solute j_s (unit $\text{mol m}^{-2} \text{s}^{-1}$) cross the membrane (Figure 1.4a), given by^{||}:

$$J = L_p \Delta P - L_p \sigma_s \mathcal{R} T \Delta c, \quad (1.11)$$

$$j_s = P_s \Delta c + (1 - \sigma_s) \bar{c} J + j_s^*. \quad (1.12)$$

On the right-hand side of the water transport eqn (1.11), the first term represents the pressure-driven flow, where L_p is the hydraulic conductivity of the membrane (unit $\text{m s}^{-1} \text{Pa}^{-1}$), the second term is the osmotic flow driven by the solute concentration difference, and σ_s is the reflection coefficient of the solute ($0 \leq \sigma_s \leq 1$)**. Physically, osmosis arises because some of the momentum associated with solute thermal agitation is taken up by the cell membrane and not by the water molecules, creating a net suction of water across the membrane to the more solute-concentrated compartment (see Box 1.3 and ref. 84).

On the right-hand side of the solute transport eqn (1.12), the first term corresponds to the passive diffusion of solute along the concentration gradient (Fick’s law type), where P_s (unit m s^{-1}) is the membrane permeability to solute. In plant membranes, both P_s and σ_s are solute dependent and can be regulated through the plasmodesmata permeability, in a complex feedback with turgor pressure.⁶⁸ The second term corresponds to the coupling between water transport and solute transport across the membrane, where \bar{c} is the mean concentration of solute across the membrane. Finally, the third term j_s^* corresponds to the molar flux of solute actively pumped against the solute gradient using specialized channels and external chemical energy. Values ranging from $j_s^* = 10^{-7}$ to $10^{-6} \text{ mol m}^{-2} \text{s}^{-1}$ are found for the

^{||}These relationships hold for non-electrolytic solutions. In the case of ions, the electric potential difference across the membrane must be added in the driving forces.

**Eqn (1.11) can be rewritten with the water potential explicitly shown as: $J = L_p \Delta \Psi + (1 - \sigma_s) \mathcal{R} T \Delta c$. The second term corresponds to the volume dragged by the solutes when they cross a non-impermeable membrane ($\sigma_s < 1$). In the extreme case where $\sigma_s = 0$ (free diffusion), we recover the fact that only a pressure gradient can induce a net flow.

potassium ion flux responsible for stomatal movement¹⁴¹ and in the motor cells of *Mimosa pudica*.¹⁵² The highest solute conductance in plant membranes is probably found in MscS-like (small conductance mechanosensitive ion channel) stretch-activated channels.⁶⁵

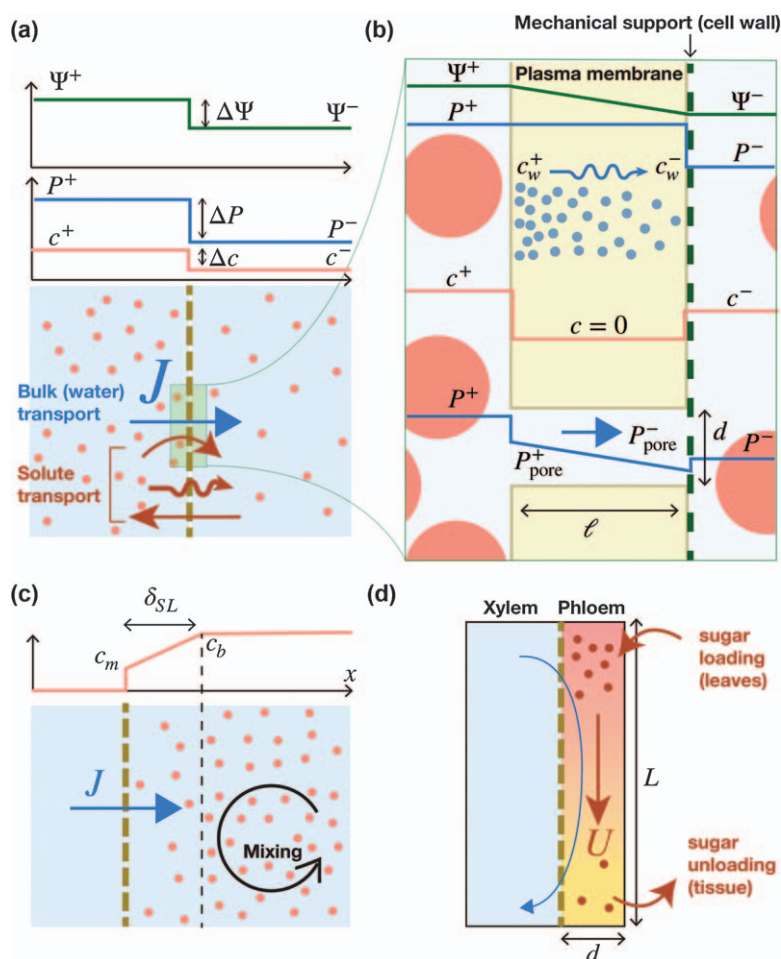


Figure 1.4 Osmotic and transmembrane flows. (a) Water and solute transport across a semi-permeable membrane driven by a gradient of water potential. Solute transport (red arrows) can be split into active transport (straight arrow) and passive transport if the membrane is leaky (undulating arrow: diffusion along gradients of concentration, curved arrow: solute carried by water flow). (b) Close-up showing two modes of water transport for an ideal semi-permeable membrane. Top: diffusive transport driven by a water concentration gradient inside a low-water-solubility membrane, such as the lipid bilayer of the plasma membrane. Bottom: pressure-driven flow inside water pores, such as aquaporins. (c) Stirring layer effects at the vicinity of a semi-permeable membrane. (d) Osmotically driven transport of sugar and Münch's mechanism.

In many situations (salts, sugar, metabolites) the reflection coefficient of the solute is close to unity and the membrane may be assumed perfectly impermeable to the solutes ($\sigma_s = 1$, $P_s = 0$). For such an ideal semipermeable membrane, the water flux across the membrane is just given by the water potential difference across the cell and the hydraulic conductivity of the membrane L_p :

$$J = L_p(\Delta P - \mathcal{R}T\Delta c) = L_p\Delta\Psi. \quad (1.13)$$

Typical values of the membrane conductivity in plant cells are $10^{-13} < L_p < 10^{-11} \text{ m s}^{-1} \text{ Pa}^{-1}$ depending on the physiological state of the cell.¹⁴⁷ These values actually reflect two distinct modes of water transport at the microscopic level (see Box 1.3 and Figure 1.4b). On the one hand, water can cross the cell membrane by molecular diffusion inside the lipid bilayer, which acts as a low-solubility medium for water. On the other hand, water can flow in bulk through selective water channels of high conductivity in the cell membrane, called aquaporins,⁹⁶ whose shape is optimized for water flow.⁵⁹ The opening and closing of these channels is under tight physiological control.

We conclude this brief survey by noting that the fluxes in eqn (1.11) and (1.12) are set by the value of the concentration jump determined exactly at the membrane. However, any osmotic flow – or solute diffusion if the membrane is leaky – tends to pile up solutes on one side of the membrane and sweep them away on the other side. The concentration difference across the membrane is then smaller than the concentration difference imposed in the bulk, which in turn reduces the osmotic flow. To minimize this effect, some mixing is necessary to homogenize the concentration field and bring the bulk concentration c_b to a distance δ_{SL} as close as possible to the membrane, called the “unstirred layer” thickness^{35,120} (Figure 1.4c). In plant cells, such mixing can be achieved thanks to intracellular flows called “cytoplasmic streaming” that are actively driven by molecular motors (see Chapter 2). If δ_{SL} is known, it is possible to estimate the real solute concentration at the membrane $c_m = c(x=0)$ by balancing, in the unstirred layer, the diffusive flux and the advection flux: $Ddc/dx \sim Jc$ with the boundary condition $c(x=\delta_{\text{SL}}) = c_b$, where D (unit $\text{m}^2 \text{s}^{-1}$) is the diffusion coefficient for the solutes and $J = L_p \mathcal{R}T c_m$ is the osmotic flux (assuming an ideal semi-permeable membrane and no pressure difference across the membrane). We deduce a transcendental equation for c_m :

$$c_m = c_b \exp - \frac{J(c_m)\delta_{\text{SL}}}{D}, \quad (1.14)$$

which can be used to estimate the reduction of osmotic flux caused by unstirring layer effects. In practice, for a typical osmotic flux $J \sim 1 \text{ } \mu\text{m s}^{-1}$ (corresponding to an osmotic pressure $\Pi \sim 1 \text{ MPa}$ with $L_p \sim 10^{-12} \text{ m s}^{-1} \text{ Pa}^{-1}$), an unstirred layer $\delta_{\text{SL}} \sim 10 \text{ } \mu\text{m}$ (a value similar to the cell width) and a coefficient of diffusion $D \sim 10^{-10} \text{ m}^2 \text{s}^{-1}$, we find that $c_m \sim 0.9 c_b$, meaning

that unstrirring layer effects on osmotic flows are likely to be small for plant cells. This may, however, not be the case for solute transport if the membrane is leaky.³⁵

1.1.3.2 Osmotically Driven Transport of Sugar and Münch's Mechanism

Osmotic flows are the basis for the building of the positive turgor pressure in plant cells discussed in Section 1.1.1. By adjusting their solute content, plant cells pump in and out water to maintain cell hydration in dry conditions or change their volume. One of the most important cell movements driven by osmosis in plants is the closing and opening of the stomata, the cellular valves that control the exchange of gas between the plant and the atmosphere at the surface of leaves.⁵⁵

Another important example of osmotically driven flow in plants is the long-distance transport of sugar (Figure 1.4d). Sugar is produced locally in leaves from photosynthesis. To ensure its transport, sugar is first loaded inside living pipe-like cells called the phloem, which are adjacent to the water-filled xylem. This high concentration of sugar in the phloem decreases its water potential and creates an osmotic flow coming from the xylem, where the water potential is larger. This inward flow creates, in turn, a positive turgor pressure at the top of the phloem and thus a pressure-driven flow that transports sugar along the phloem toward the places where it is unloaded and used for growth or storage. This mechanism was first proposed by Münch in 1930.¹⁰⁷ The velocity of the flow transporting sugar is controlled by the Münch number:

$$\text{Mu} = \frac{64\eta L_p L^2}{d^3}, \quad (1.15)$$

where L_p is the membrane permeability of the phloem tube, L the length of the phloem and d its diameter. For $\text{Mu} \gg 1$, the viscous resistance of the phloem tube dominates. The mean flow velocity is then given by the Hagen–Poiseuille's law (see eqn (1.9)): $U = Q/(\pi d^2/4) \sim d^2/(32\eta)cRT/L$, where c is the sugar concentration. By contrast for $\text{Mu} \ll 1$ the dissipation from the cell membrane dominates and the velocity U is imposed by the water flux across the membrane $J = L_p cRT$ (see eqn (1.13)) and volume conservation $U\pi d^2/4 \sim \pi L d J$, giving $U \sim (4L/d)L_p cRT$. The Münch number is just the ratio of these two limiting case velocities. A typical value of the Münch number for the phloem is $\text{Mu} \sim 10^{-4} \ll 1$ (taking $L = 1$ cm, the typical length of a leaf stem, $d \sim 20$ μm , $\eta \sim 2 \times 10^{-3}$ Pa s, $L_p \sim 10^{-13}$ m s⁻¹ Pa⁻¹ and $cRT \sim 1$ MPa⁷⁵), which gives a phloem's velocity $U \sim 0.2$ mm s⁻¹ consistent with observation.

The transport of sugar along the phloem is governed by an advection-diffusion equation:

$$\frac{\partial c}{\partial t} + U \nabla c = D \Delta c, \quad (1.16)$$

where D [unit $\text{m}^2 \text{s}^{-1}$] is the diffusion coefficient of sugar molecules in water (here no sink or source of sugar are considered along the path). The ratio of the advective to the diffusive term is quantified by the Péclet number:

$$\text{Pe} = \frac{UL}{D}. \quad (1.17)$$

Taking for the diffusion coefficient of sucrose in water $D = 5 \times 10^{-10} \text{ m}^2 \text{s}^{-1}$, $L = 1 \text{ cm}$ (leaf stem) and $U = 0.2 \text{ mm s}^{-1}$ gives $\text{Pe} = 4 \times 10^3 \gg 1$. Therefore, advection by the osmotic flow clearly dominates diffusion in the long-distance sugar transport. In-depth discussion of this fascinating mode of transport can be found in ref. 75.

1.1.4 Evaporation and Vapor Diffusion

We have seen that the water potential within plant tissues is generally negative, with values ranging from 0 MPa for roots immersed in a well-watered soil to few -MPa at the tops of trees or for plants living in arid or saline environments. However, the water potential of the atmosphere is much lower, with $\Psi_{\text{vap}} = -70 \text{ MPa}$ for a typical 60% humidity (see eqn (1.3)). Water loss by evaporation is thus a critical issue faced by all terrestrial plants, which they partly solve by covering most of their surfaces with a waxy hydrophobic layer called cuticle (Figure 1.5a). However, some gas exchange with the atmosphere must be maintained in order to capture the carbon dioxide and other gases necessary for photosynthesis and plant metabolism. This exchange occurs on the surface of leaves through specialized pores called stomata. Still, a trade-off is required as many water molecules are lost through evaporation when the stomata open (typically 100 kg of water are lost for 1 kg of glucose synthesized in plants, see ref. 112), which is achieved by fine regulation of stomatal function. A general review on leaf hydraulics, from water movements through the leaf xylem to transport in the air space between the leaf cells can be found in ref. 137. The complex interplay between biological signaling and stomata dynamics is discussed in ref. 88. Here we focus on the basic physics of vapor diffusion in relation to plant evaporation.

1.1.4.1 Fick's Law

Evaporation at the liquid/air interface within leaves and diffusion of water through the stomata represent the final mode of water transport in plants as

Box 1.3 Osmosis and water transport across cell membranes.

We have seen that water transport across an ideal semi-permeable membrane is characterized by a single parameter, the hydraulic permeability of the membrane L_p , which relates the bulk flux J to the difference in water potential $\Delta\Psi$, regardless of whether it comes from a hydrostatic ΔP or osmotic $\mathcal{RT}\Delta c$ pressure gradient (eqn (1.13)). Microscopically, however, L_p can describe two very different modes of water transport, which we briefly discuss here (more details can be found in the excellent book by Finkelstein⁴⁷).

The first situation concerns a membrane of low solubility for water, which typically corresponds to the lipid bilayers of the plasma membrane (Figure 1.4b). In this “oil membrane” model, the concentration of water molecules in the membrane is low, and water crosses the membrane from one side to another mainly through diffusion, following a water concentration gradient inside the membrane. Fick’s law for the molar flux of water inside the membrane reads $j_{\text{water}} = D_w^{\text{oil}}(c_w^+ - c_w^-)/\ell$, where D_w^{oil} is the diffusion coefficient of water molecules in the oily membrane, ℓ is the membrane thickness and $(c_w^+ - c_w^-)$ is the difference in water molar concentration at both end of the membrane. This molar flux is associated with a volume flux of water:

$$J = \nu_w j_{\text{water}} = D_w^{\text{oil}} \nu_w \frac{c_w^+ - c_w^-}{\ell}. \quad (1.18)$$

It is possible to relate this concentration difference inside the membrane to the external water potential difference $\Delta\Psi$, and thus to relate L_p and D_w^{oil} . Indeed, the continuity of the water potential at the interface of both membranes implies that (see Figure 1.4b for notation):

$$P^+ - c^+ \mathcal{RT} = -\frac{\Delta\mu^0}{\nu_w} + \frac{\nu_{\text{oil}}}{\nu_w} P^+ + \frac{\mathcal{RT}}{\nu_w} \ln(c_w^+ \nu_{\text{oil}}), \quad (\text{left}) \quad (1.19)$$

$$-\frac{\Delta\mu^0}{\nu_w} + \frac{\nu_{\text{oil}}}{\nu_w} P^+ + \frac{\mathcal{RT}}{\nu_w} \ln(c_w^- \nu_{\text{oil}}) = P^- - c^- \mathcal{RT}. \quad (\text{right}) \quad (1.20)$$

Here, we have used the expression of the chemical potential of water inside the oily membrane in the dilute limit, $\mu_w^{\text{oil}} = \mu_w^{0,\text{oil}} + \nu_{\text{oil}} P + \mathcal{RT} \ln c_w \nu_{\text{oil}}$, where ν_{oil} is the molar volume of the membrane and $\Delta\mu^0 = \mu_w^0 - \mu_w^{0,\text{oil}}$ is the difference between the chemical potential of pure water in the reference state (atmospheric pressure at ambient temperature) and the chemical potential of water in the membrane in the reference state and for a water activity equal to one.⁴⁷ Importantly, since there is a difference of hydrostatic pressure across the membrane, an external “grid” (e.g. cell wall) must exist on the right-hand side of the membrane in order to balance the pressure difference. As a result, the hydrostatic pressure inside

the whole membrane is uniform and equal to the left-hand side pressure P^+ . Assuming that $v_w \Delta \Psi / \mathcal{R}T \ll 1$, one may linearize the exponential and obtain:

$$c_w^+ - c_w^- = \frac{v_w c_0}{\mathcal{R}T} (P^+ - c^+ \mathcal{R}T - P^- + c^- \mathcal{R}T) = \frac{v_w c_0}{\mathcal{R}T} \Delta \Psi, \quad (1.21)$$

where $c_0 = (1/v_{oil}) \exp[(\Delta \mu + P^+ (v_w - v_{oil}))/\mathcal{R}T]$ is the molar concentration of water in the membrane for a membrane in equilibrium with pure water in the reference state. Introducing eqn (1.21) in (1.18) and identifying with the transport eqn (1.13) gives the following expression for the hydraulic permeability in the case of lipid membranes:

$$L_p^{\text{lipid bilayer}} = \frac{D_w^{\text{oil}} v_w^2 c_0}{\mathcal{R}T \ell}. \quad (1.22)$$

Taking $c_0 = 40 \text{ mol m}^{-3}$, $D_w^{\text{oil}} = 10^{-10} \text{ m}^2 \text{ s}^{-1}$ and $\ell = 3 \text{ nm}$ (see ref. 47) gives $L_p \sim 10^{-13} \text{ m s}^{-1} \text{ Pa}^{-1}$, a correct order of magnitude for the permeability of lipid bilayer membranes.

The other situation corresponds to the existence of water pores inside the membrane, such as aquaporin channels, which let water move freely but exclude large solutes or ions. In this case, water transport does not occur through diffusion but more like a pressure-driven bulk flow in a pipe, although the molecular size of the pore may complicate the description.^{47,59} The gradient of hydrostatic pressure driving the flow inside the pore can be estimated as before, by assuming the continuity of the water potential on both sides of the pore. Since solutes are excluded from the pore, the sharp drop of solute concentration on both sides of the pore induces a sharp drop of hydrostatic pressure, such that $P_{\text{pore}}^+ = P^+ - c^+ \mathcal{R}T$ and $P_{\text{pore}}^- = P^- - c^- \mathcal{R}T$ (Figure 1.4b). The gradient of hydrostatic pressure in the water pore is thus $(P_{\text{pore}}^+ - P_{\text{pore}}^-) \ell = \Delta \Psi / \ell$. We recover that, although the flow in the pore is driven by a purely hydrostatic pressure gradient, its value is given by the jump of water potential outside the pore, as expected from the transport eqn (1.13). Assuming Hagen–Poiseuille’s law to hold (eqn (1.9)) and a surface density of n_s pores per unit surface, the total water flux per unit membrane area is $J = n_s (\pi d^4 / 128 \eta) (\Delta \Psi / \ell)$. Identifying this expression with the transport eqn (1.13) gives the following expression for the hydraulic permeability in the case of transports through water pores:

$$L_p^{\text{water pores}} = \frac{n_s \pi d^4}{128 \eta \ell}. \quad (1.23)$$

Taking $n_s = 10^6 \text{ pores m}^{-2}$, $d = 0.2 \text{ nm}$, $\ell = 3 \text{ nm}$ and $\eta = 10^{-3} \text{ Pas}$ gives again $L_p \sim 10^{-13} \text{ m s}^{-1} \text{ Pa}^{-1}$.

it moves from the soil to the atmosphere. The diffusive flux of water molecule in a humid atmosphere j_{water} (number of moles crossing a unit area per unit time, or $\text{mol m}^{-2} \text{s}^{-1}$) is given by Fick's law:

$$j_{\text{water}} = -D_w \nabla c_w, \quad (1.24)$$

where $D_w = 2.4 \times 10^{-5} \text{ m}^2 \text{s}^{-1}$ is the diffusion coefficient of the water molecule in air at 20°C and c_w is the molar concentration of water in air (unit mol m^{-3}). Fick's law can be equivalently expressed in term of the vapor pressure gradient, using the gas state equation, $P_{\text{vap}} = c_w \mathcal{R}T$, or in term of the water potential of the vapor using eqn (1.3):

$$j_{\text{water}} = -\frac{D_w}{\mathcal{R}T} \nabla P_{\text{vap}} = -\left[\frac{D_w v_w P_{\text{sat}}(T)}{(\mathcal{R}T)^2} \exp\left(\frac{v_w}{\mathcal{R}T} \Psi\right) \right] \nabla \Psi. \quad (1.25)$$

However, when expressed in term of the water potential, the coefficient of proportionality between the water molecular flux and the gradient of water potential is not constant but varies exponentially as: $\exp\left(\frac{v_w}{\mathcal{R}T} \Psi\right)$. Hence, for a given gradient of water potential, a dry atmosphere (very negative Ψ) has a much lower “conductivity” than a humid one ($\Psi \simeq 0$).

1.1.4.2 Evaporation from Stomata

As a first example of the application of Fick's law, we consider evaporation from a surface of pure water subjected to a side wind of velocity U_{wind} in an atmosphere of relative humidity $[\text{RH}]_{\text{atm}} = P_{\text{vap}}/P_{\text{sat}}(T)$ (Fig. 1.5b). A diffusive boundary layer of size $\delta \sim \sqrt{D_w L / U_{\text{wind}}}$ developed above the surface, where L is the typical surface size. The molecular flux of water is thus given by:

$$j_{\text{water}}^{\text{BL}} \sim D_w \frac{c_{\text{sat}} - c_{\text{atm}}}{\delta} \sim \frac{D_w P_{\text{sat}}(T)}{\mathcal{R}T} (1 - [\text{RH}]_{\text{atm}}) \sqrt{\frac{U_{\text{wind}}}{D_w L}}. \quad (1.26)$$

Taking a wind velocity $U_{\text{wind}} = 10 \text{ m s}^{-1}$ and a lateral size $L = 10 \text{ cm}$ (leaf size) gives a diffusive boundary layer of thickness $\delta \sim 0.5 \text{ mm}$. For a very dry atmosphere ($[\text{RH}]_{\text{atm}} \sim 0$), this gives a molecular flux $j_{\text{water}} \simeq 10^{-2} \text{ mol m}^{-2} \text{s}^{-1}$ and an evaporative mass flux $J_m = M_w j_{\text{water}} \simeq 2 \times 10^{-4} \text{ kg m}^{-2} \text{s}^{-1}$, where $M_w = 18 \text{ g mol}^{-1}$ is the molar mass of water. This value is surprisingly close to the maximal evaporating rate reported per surface leaf area in plants.⁷⁵ This is all the more remarkable that stomatal pores covers only 1–10% of the leaf surface, the rest being almost impermeable to evaporation.

To understand this feature, we consider an ideal leaf made of a flat impermeable sheet perforated with holes (stomata) of pore size a (Figure 1.5c). The sheet is in contact with pure water at the bottom and placed in an atmosphere of water vapor concentration c_{atm} above. For an isolated stomata,

the size of the diffusive boundary layer is fixed by the pore size $a^{\dagger\dagger}$. Assuming that stomata do not interact with each other, the total evaporation rate of the leaf per unit area is thus:

$$j_{\text{water}}^{\text{stomata}} \sim n_s a^2 D_w \frac{c_{\text{sat}} - c_{\text{atm}}}{a} \sim n_s a D_w (c_{\text{sat}} - c_{\text{atm}}). \quad (1.27)$$

where n_s is the number of stomata per unit leaf area. We find that the evaporative flux from the leaf is equal to the evaporative flux from a surface of pure water ($j_{\text{water}}^{\text{stomata}} \sim j_{\text{water}}^{\text{BL}}$) when $n_s \sim 1/(a\delta)$ or $\phi_s \sim a/\delta$, where $\phi_s \sim n_s a^2$ is the surface fraction covered by the stomata. Taking $\delta \sim 1$ mm and $a \sim 10$ μm , we find that this condition is fulfilled with stomata covering only 1% of the leaf area ($\phi_s = 0.01$). Indeed, due to their small size, stomata impose a diffusion length scale much smaller than the air boundary layer, resulting in high local evaporative gradients that compensate for their small area.

Eqn (1.27) predicts the paradoxical result that, for a sufficiently high concentration of stomata, the evaporative flux from the leaf could be greater than that from a pure water surface. This is because we have assumed that the external vapor concentration fixing the stomatal vapor flux is c_{atm} . This assumption is valid only if the distance between stomata, $s \sim 1/\sqrt{n_s} \sim a/\sqrt{\phi_s}$, is much larger than the air boundary layer δ . In practice, however, $s \ll \delta$. In this situation, the total resistance to evaporation from the leaf, defined as $R_{\text{Leaf Evap}} = (c_{\text{sat}} - c_{\text{atm}})/j$, is the sum of the stomatal resistance $R_{\text{stomata}} \sim 1/(n_s a D_w) \sim a/(\phi_s D_w)$ and the resistance of the air boundary layer $R_{\text{BL}} = \delta/D_w$ (Figure 1.5d). We find that both resistances are equal when $\phi_s \sim a/\delta$, recovering the previous condition. A detailed discussion of the role of stomata interaction on leaf vapor diffusion can be found in ref. 89.

1.1.4.3 Diffusive versus Bulk Transport: Plants as Water Valve

As a second application of Fick's law, it is instructive to compare, for the *same* difference in water potential, the mass of water transported in bulk by a pressure gradient with that transported in vapor form by diffusion in a humidity gradient (Figure 1.5e). According to Poiseuille's law (eqn (1.9)), the mass bulk flow through a pipe of diameter d and length L is $Q_{\text{m}}^{\text{bulk}} = \rho(\pi d^4/128\eta) \times (\Delta\Psi/L)$, where ρ is the density of the liquid water, η is the water viscosity and $\Delta\Psi = \Delta P$ is the pressure difference across the pipe. On the other hand, transport of water vapor in the same pipe by diffusion from a vapor at saturation to an external atmosphere of humidity $[\text{RH}]_{\text{atm}}$ gives, using Fick's law, a diffusive mass flux: $Q_{\text{m}}^{\text{diffusion}} = M_w(\pi d^2/4)(D_w/RT)P_{\text{sat}}(T)[(1 - [\text{RH}]_{\text{atm}})/\Delta\Psi] \times (\Delta\Psi/L)$. Therefore, for the same gradient of water potential, the ratio of the bulk to diffusive transport is:

$$\frac{Q_{\text{m}}^{\text{bulk}}}{Q_{\text{m}}^{\text{diffusion}}} = \frac{\rho \mathcal{R} T d^2 \Delta\Psi}{32\eta M_w D_w P_{\text{sat}}(T)(1 - [\text{RH}]_{\text{atm}})}. \quad (1.28)$$

^{††}This is valid as long as $a \ll \delta_v$ where $\delta_v \sim \sqrt{\nu L / U_{\text{wind}}}$ is the viscous boundary layer and $\nu \sim 10^{-5} \text{ m}^2 \text{ s}^{-1}$ is the air kinematic viscosity.

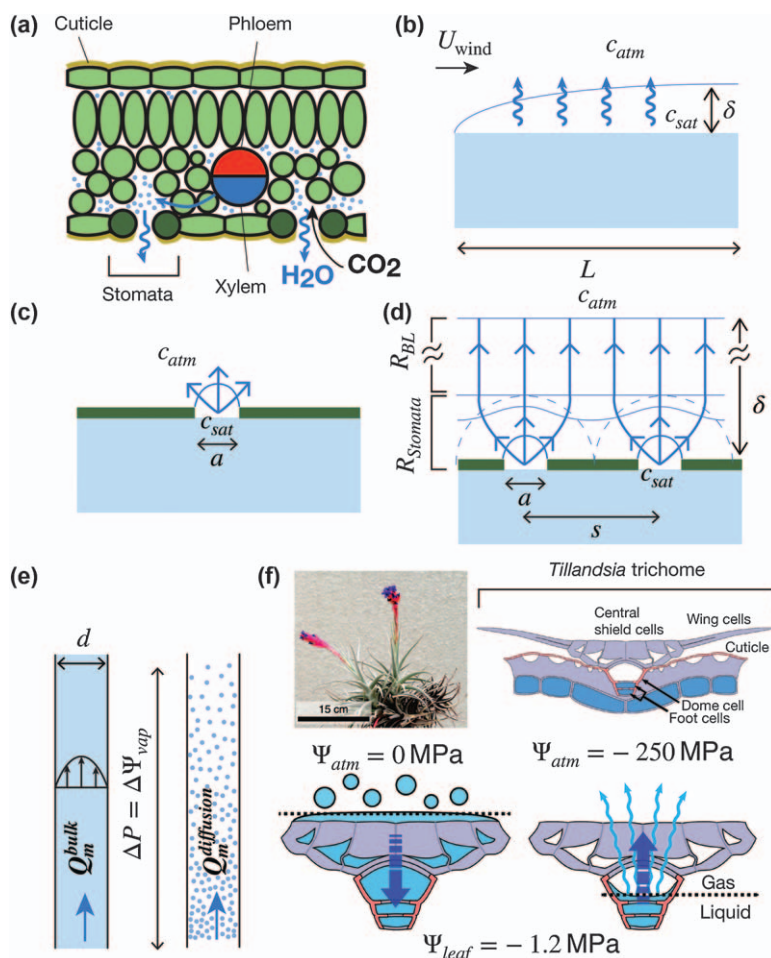


Figure 1.5 Evaporation in plants. (a) Cross-section of a leaf showing the water transport path from the xylem (liquid state) to the stomata (gas state). (b) Diffusive air boundary layer above an evaporative bath of water subjected to a cross-wind. (c) Evaporation from an isolated stomata modeled as a hole of size a in an impermeable plate. (d) Pattern of vapor diffusion above a “leaf” made of several “stomata”. Thin solid lines give show the iso-concentration of vapor while thick solid lines show the direction of the vapor flux. (e) Bulk flow in the liquid state *versus* diffusive transport in the gas state for a given water potential difference $\Delta P = \Delta \Psi_{\text{vap}}$. (f) Asymmetric water transport (“water valve”) at the trichomes of the plant *Tillandsia aeranthos* (photo) living in the Atacama desert in Chile. Reproduced from ref. 128, <https://doi.org/10.1038/s41467-019-14236-5>, under the terms of the CC BY 4.0 license <https://creativecommons.org/licenses/by/4.0/>.

Taking $d \sim 1 \mu\text{m}$ and a water potential difference for an atmosphere of 50% humidity gives: $Q_m^{\text{bulk}}/Q_m^{\text{diffusion}} \sim 10^7$! This shows that, even in very small conduits, bulk transport driven by a pressure gradient in the liquid

state is much more efficient than vapor diffusion driven by a humidity gradient.

This simple principle is harnessed by the plant *Tillandsia*, which lives in the Atacama desert in Chile, to design an asymmetrical “water valve” on the surface of its leaves¹²⁸ (Figure 1.5f). The Atacama desert is probably the driest place on Earth, with a humidity as low as 15%, which corresponds to a water potential $\Psi_{\text{atm}} = -250$ MPa. However, a few days a year, fog from the coast brings a very humid atmosphere full of tiny droplets of liquid water ($\Psi_{\text{atm}} \sim 0$ MPa). These droplets condense on the very hydrophilic surface of *Tillandsia* leaves and are absorbed by the leaf cells through osmosis, due to their high concentration of solute which creates a negative water potential Ψ_{leaf} of about -1 MPa. Remarkably, although the difference in water potential causing water absorption during wet periods ($\Delta\Psi_{\text{abs}} = |\Psi_{\text{atm}} - \Psi_{\text{leaf}}| = +1$ MPa) is a hundred times *smaller* than the difference in water potential causing water evaporation during dry periods ($\Delta\Psi_{\text{evap}} = +249$ MPa), the absorption flow rate is found to be a hundred times *greater*.¹²⁸ This corresponds to a difference in effective conductance $Q/\Delta\Psi$ between the humid and dry states a few thousands.

This strong asymmetry is explained by the existence of specialized structures at the surface of *Tillandsia*'s leaves, called trichomes, where water exchanges takes place.¹²⁸ These trichomes consist of a row of empty dead cells covered by a very thick cell wall, which separate the leaf cells from the atmosphere (Figure 1.5f). During wet periods, the wall and dead cell cavities are completely soaked with liquid water due to their hydrophilic nature; absorption then occurs in the liquid state, through an osmotically driven bulk flow limited by the leaf cell membrane permeability. By contrast, during the dry periods, the liquid/vapor interface shifts within the trichome. Transport to the outside then occurs by diffusion in the vapor form which, as we have seen, is very inefficient.

1.2 Solids

So far in the chapter, we have considered plants as rigid and static containers, in which water and solutes are transported according to the laws of thermodynamics and fluid mechanics. However, in order to absorb water, grow or generate movement, the cells and tissues of plants must deform. This chapter discusses the relationships between stress and deformation in the plant solid body, and how this deformation is coupled with water transport. Other examples of fluid–structure interaction in plants are discussed in Chapter 2.

1.2.1 The Wall Stress and the Force Balance

1.2.1.1 Force Balance at the Cellular Level

The solid phase of plants is essentially made by the wall material that surrounds all plant cells (Box 1.1 and Figure 1.1). Plant cells have two types of wall.¹⁵⁵ Young growing cells and the mature cells of some tissues (leaf) are surrounded by a thin primary cell wall made of stiff cross-linked cellulose microfibrils

embedded in a highly hydrated matrix of polysaccharides (hemicelluloses and pectins mainly),^{32,33,72} whose thickness h is typically between 0.1 μm and a few μm . When growth stops, a thicker and more rigid secondary cell wall of lignin and other woody components may be added, giving additional strength.

Under physiological conditions, the wall of living cells is stretched by the internal, osmotically induced, turgor pressure (see Section 1.1). From a mechanics perspective, a plant cell thus behaves like a pressurized thin shell (Figure 1.6a). The tensile stress σ_{wall} (force per unit area) stretching the wall can be estimated by modeling the cell as a spherical shell of radius R and uniform wall thickness $h \ll R$ under a pressure difference P between the inside and outside. The balance of force on the half-shell imposes that the external pressure force $\pi R^2 P$ is equal and opposite to the tensile force in the wall integrated along the wall perimeter $2\pi R h \sigma_{\text{wall}}$ (Figure 1.6a), giving:

$$\sigma_{\text{wall}} \sim \frac{R}{2h} P. \quad (1.29)$$

This Young-Laplace-like relationship shows that the tensile stress in the wall may be much larger than the turgor pressure due to the geometrical amplification factor R/h . Taking a typical plant cell geometry $R = 10 \mu\text{m}$, $h = 1 \mu\text{m}$ and turgor pressure $P = 0.5 \text{ MPa}$ gives $\sigma_{\text{wall}} = 2.5 \text{ MPa}$, which is much larger than the maximal tensile stress generated by animal muscle ($T_{\text{muscle}} \sim 0.2 \text{ MPa}$ ¹³⁴).

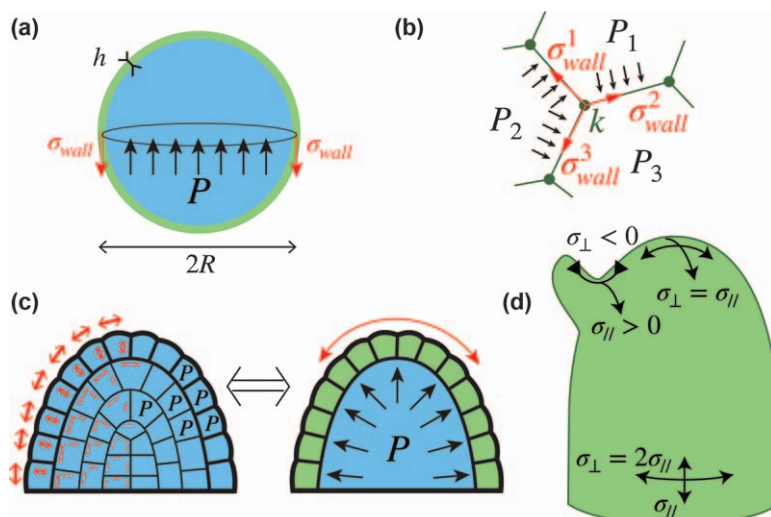


Figure 1.6 Force and stress balance in plant tissues. (a) Force balance in a cell viewed as a pressurized shell in order to compute the wall stress σ_{wall} . (b) Vertex model of a plant tissue (redrawn and adapted from ref. 26). (c) Tissue-tension approximation: the epidermis, which is much stiffer than the inner cells, carries most of the turgor-driven wall stress (red arrows). The left-hand drawing is inspired by ref. 117. (d) Surface stress distribution in the tissue-tension approximation, depending on the local geometry of the organ.

We will see that this stress level is enough to significantly deform the plant cell wall and change its cell volume.

1.2.1.2 Force Balance in Plant Tissues

The balance of forces written here for an isolated cell can be generalized to a tissue composed of several cells. In plants, each cell wall is glued to its neighbor by an adhesive layer called the middle lamella, which prevents the cells from sliding against each other or becoming detached (the situation of invasive growth, discussed in detail in Chapter 7, is an exception). However, unlike the case of an isolated cell, the balance of forces is generally not sufficient to determine the stress distribution in all the walls of the tissue. Even when the cell geometry and the turgor pressure are known, additional knowledge of the constitutive relation of the cell wall is usually required (see Sections 1.2.2 and 1.2.4). In most situations, the complete computation of the tissue stress can only be done by means of heavy and expensive numerical simulations, using for example Finite Element Methods.¹⁵ Modeling plant solid mechanics at the tissue and organ level thus often relies on simplified models.

The first class of model, broadly called cell-based models, considers the discrete nature of cells with different degrees of approximation. Of these methods the vertex model is one of the most popular.^{26,63,93} In its two-dimensional version, the tissue is modeled as a collection of polygons representing cells, in which linear segments representing the wall are in tension and connected to vertices representing the wall junction (Figure 1.6b). The global force balance implies that, at each vertex k , the (half) sum of the pressure difference force at each face adjacent to k balances the sum of the wall tension applied to k . A detailed presentation of vertex-like approaches is given in Chapter 3.

The second class of model uses continuum mechanics to define an average stress tensor σ which integrates both the wall stress and the turgor pressure at the tissue level (see Chapter 3 for a detailed discussion of the averaged stress tensor in plant tissue). In the absence of body forces, the internal force balance is then given by:

$$\nabla \cdot \sigma = 0. \quad (1.30)$$

1.2.1.3 The Tissue–Tension Assumption: Plant Tissues as Pressurized Shells

An approximation often used to describe stresses in plant tissues is based on the fact that epidermal cells are generally much stiffer than the cells of the underlying tissue, due to their small size and thick outer wall. The epidermal layer is then assumed to support most of the turgor pressure generated by the internal cells and the entire tissue is modeled as a pressurized shell^{14,67,86} (Figure 1.6c). Using this tissue–tension assumption and neglecting the bending stiffness of the epidermis, the force balance in the

direction perpendicular to the epidermis reduces to a generalized Young–Laplace equation:¹⁵⁷

$$h \left(\frac{\sigma_{\parallel}}{R_{\parallel}} + \frac{\sigma_{\perp}}{R_{\perp}} \right) = P. \quad (1.31)$$

Here $(\sigma_{\parallel}, \sigma_{\perp})$ are the local principal in-plane stresses in the epidermis; $(R_{\parallel}, R_{\perp})$ are the local principal radius of curvature of the organ's surface, and P represents the turgor pressure of the cells in the bulk below the epidermis. This equation must be complemented by the force balance in the plane of the shell given by $(\partial\sigma_{\parallel}/\partial s_{\parallel} = 0)$ and $\partial\sigma_{\perp}/\partial s_{\perp} = 0$, where $(s_{\parallel}, s_{\perp})$ is the arc-length along the principal directions. The pressurized-shell model has been widely used in the context of plant morphogenesis to determine the tissue stress distribution in organs of various shapes, such as the shoot apical meristem or in leaves^{63,69,138} (Figure 1.6d). For a spherical cap of radius R like the tip of a growing shoot ($R_{\parallel} = R_{\perp} = R$), the tissue stress is uniform and we recover the relationship (1.29): $\sigma_{\perp} = \sigma_{\parallel} = PR/2h$. For a cylinder of radius R like a stem or a root ($R_{\parallel} = \infty, R_{\perp} = R$), eqn (1.31) predicts that the perpendicular, hoop stress is twice the longitudinal stress: $\sigma_{\perp} = 2\sigma_{\parallel} = PR/h$. Finally, for a saddle crease geometry like at the cusp of a bud ($R_{\perp} = -r < 0$ and $R_{\parallel} = +R \gg r$), one of the stresses is then compressive: $\sigma_{\perp} \approx -Pr/h$ while the other is in tension: $\sigma_{\parallel} \approx +PR/h$ (Figure 1.6d). Hence, although the internal driving force – the turgor pressure – is isotropic, stress anisotropy is more the rule than the exception in plants.

The tension of the epidermal tissue predicted by the pressurized shell model is an example of residual stress, *i.e.* a non-zero internal stress in a body at equilibrium and in the absence of external loading. Such residual stresses are common in plants due to wall adhesion and the absence of sliding between cells. In fact, any material inhomogeneity induced by gradients of structure, elasticity, swelling rate or growth in a plant tissue is susceptible to generate residual stresses, which may or may not be resolved by tissue buckling or stress relaxation. The feedback between the tissue shape, residual stress, and the biological response (growth law, mechano-transduction) is central to plant morphogenesis and development.¹⁴

1.2.2 Elasticity

1.2.2.1 Hooke's Law and Cell Wall Elasticity

As the plant wall is a living material, its mechanical description must be approached with caution, especially for growing cells. However, as long as the deformations are small enough (typically less than 5–10% in living cells), and the timescales of observation not too large, the cell wall may be approximated as an elastic solid. The simplest elastic constitutive law is Hooke's law, in which deformations are reversible and proportional to the applied stresses. For uniaxial deformation, Hooke's law reduces to:

$$\sigma = E\varepsilon_{\text{el}}, \quad (1.32)$$

where $\varepsilon_{\text{el}} = \Delta L/L$ is the elastic deformation or elastic strain and E (unit Pa) is the Young's modulus of the material (Figure 1.7a). The Young's modulus is a measure of the stiffness or compliance/softness of the material: the larger E is the stiffer the material, while the lower E is the more compliant or soft it is.

As a first application of Hooke's law, we can calculate the reversible volume change ΔV induced by a change in turgor pressure ΔP in a plant cell modeled as a thin spherical shell of thickness $h \ll R$ (Figure 1.7b). The force balance implies $\sigma_{\text{wall}} = (R/2h)P$ (eqn (1.29)) and Hooke's law can be written approximately as follows^{††}: $\sigma_{\text{wall}} \approx E_{\text{wall}}\varepsilon_{\text{el}} = E_{\text{wall}}(R - R_0)/R_0$, where E_{wall} is the Young's modulus of the wall and R_0 the radius of the cell in its rest state when the turgor pressure $P = 0$. Identifying these two expressions and assuming small deformation $(R - R_0) \ll R_0$ gives: $\Delta P \approx (2h/R)E_{\text{wall}}(\Delta R/R) \approx (2h/3R)E_{\text{wall}}(\Delta V/V)$. The coefficient of proportionality of this pressure/volume relationship is called the cellular bulk modulus B_{cell} (unit Pa):

$$B_{\text{cell}} = V \frac{\Delta P}{\Delta V} \approx \frac{2h}{3R} E_{\text{wall}}. \quad (1.33)$$

The cellular bulk modulus determines the water storage capacity of the cells and, as we shall see, controls the timescale of cell swelling. For xylem cells under negative pressure, it also influences the dynamics of cavitation, as discussed in Chapter 4. Importantly, the cellular bulk modulus is a measure of the Young's modulus E_{wall} of the cell wall, up to a geometric factor $\sim h/R$. Measurements of B_{cell} in a wide variety of cells has been made using the cell pressure probe described in Box 1.2.^{30,80,151} A typical value for a growing plant cell is $B_{\text{cell}} \sim 5$ MPa. Using eqn (1.33) for a plant cell of thickness $h \sim 1 \mu\text{m}$ and radius $R \sim 10 \mu\text{m}$ gives $E_{\text{wall}} \sim 75$ MPa. This order of magnitude is consistent with direct measurements of cell wall Young's modulus using tensile assays, which gives $E_{\text{wall}} \sim 50\text{--}150$ MPa for onion epidermal walls¹⁶⁷ (Figure 1.7c). The Young's modulus of the wall is even larger in giant algal cells ($E_{\text{wall}} \sim 0.5\text{--}2$ GPa¹²⁵) and can exceed 25 GPa for wood fibers.⁵⁷

Of course, the real mechanical behavior of the cell wall is more complex than the ideal Hooke's law considered here. First, the wall of living cells typically exhibits a nonlinear strain-hardening behavior, *i.e.* an increase of Young's modulus with strain, together with a dissipative behavior (viscoelasticity, plasticity),^{70,78,151,167} as found in other polymeric and gels materials (Figure 1.7c). Second, the mechanical response of the cell wall is generally anisotropic, with Young's modulus being much larger in the direction parallel to the mean orientation of the stiff cellulose microfibrils than in their perpendicular direction. Therefore, even for an isotropic loading such as that imposed by the internal turgor pressure, the deformation of a cell is generally

^{††}For this geometry and assuming an isotropic and homogeneous material, Hooke's law in the plane of the shell also involves Poisson's ratio ν of the material ($-1 \leq \nu \leq 0.5$). The exact expression of the cellular bulk modulus in this case is $B_{\text{cell}} = [2h/(3(1 - \nu)R)]E_{\text{wall}}$; see ref. 87.

non-isotropic. This anisotropy, combined with the microscopic heterogeneity of the wall, makes the characterization of the wall by a single Young's modulus too simplistic. For example, wall stiffness deduced from indentation methods using very small probes (sub-micrometer in size) are generally much lower (of the order of few MPa^{98,166}) than those obtained from tensile micro-machines or inferred from the value of the cellular bulk modulus. This is because indentation at nanoscales primarily probes the transverse elastic properties of the wall and the polysaccharide matrix between the cellulose nanofibrils, rather than in-plane global tensile properties.¹⁶⁶

1.2.2.2 Elasticity of a Single Cell

The cellular bulk modulus (eqn (1.33)) characterizes the elastic response of a plant cell to volume change, *i.e.* when the cell wall is forced to stretch further during the deformation. It is interesting to study a situation of cell deformation without change of stretch, such as a single turgid cell squeezed between two plates by a displacement δ . When the internal turgor pressure P is high and the cell wall thickness is thin ($h \ll \delta$), the problem is similar to that of a squeezed elastic balloon (Figure 1.7d). The force then mainly comes from the internal pressure acting against the plates: $F \sim P\pi a^2$, where a is the radius of the contact area between the cell and the plates. Assuming that δ is small compared to the radius of the cell R gives the geometrical relation $a^2 \sim 2R\delta$ and thus a linear relationship between the force and the displacement: $F \sim 2\pi RP\delta$. From this result, one can define an effective external stress acting on the cell $\sigma = F/(\pi R^2)$, an effective elastic strain: $\epsilon_{\text{el}} = \delta/R$ and thus an apparent Young's modulus of the cell $E_{\text{cell}} = \sigma/\epsilon_{\text{el}}$ given by:

$$E_{\text{cell}} \sim 2P. \quad (1.34)$$

Interestingly, this apparent Young's modulus depends on the turgor pressure but not on the cell wall elasticity, a property that can be used to infer the turgor pressure in experiments on single cells^{41,91} (see Box 1.2). When the turgor pressure drops to zero, the apparent cell Young's modulus predicted by eqn (1.34) vanishes. In reality, there is always a small elastic resistance coming from the bending of the cell wall, which we have ignored previously. The force needed to bend a plate of size R and thickness h over a displacement δ is $F \sim E_{\text{wall}}(h^3/R^2)\delta$,⁸⁷ yielding an apparent bending cell modulus $E_{\text{bending}} \sim [F/(R^2)]/(\delta/R)$ given by:

$$E_{\text{bending}} \sim \left(\frac{h}{R}\right)^3 E_{\text{wall}}. \quad (1.35)$$

1.2.2.3 Elasticity of Plant Tissues

The previous analysis at the cellular level is helpful to understand the relationship between the macroscopic Young's modulus of a multicellular turgid

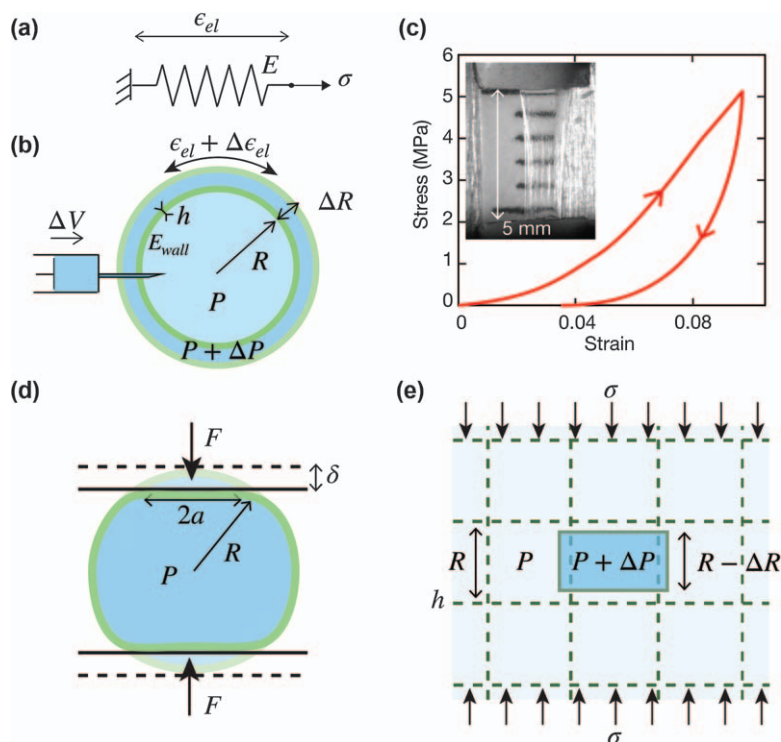


Figure 1.7 Elasticity. (a) Mechanical model of Hooke's law. (b) Pressure–volume relationship for a single cell in the elastic regime, characterized by the cellular bulk modulus $B_{\text{cell}} = V(\Delta P/\Delta V) \approx (h/R)E_{\text{wall}}$. (c) Stress–strain relationship for onion epidermal walls during a loading and unloading cycle in a tension assay. Adapted from ref. 167 with permission from AAAS, Copyright © 2021 The Authors. Photo: Onion epidermal strip stretched by ~10% (image credit: Daniel Cosgrove). (d) Elasticity of a single plant cell squeezed between two rigid plates, yielding an apparent cell Young's modulus $E_{\text{cell}} \sim P$. (e) Elasticity of an ideal plant tissue. Under compression, the cell wall is stretched and the turgor pressure changes, yielding an effective tissue Young's modulus $E_{\text{tissue}} \sim B_{\text{cell}}$.

plant tissue and the microscopic properties of its constituents (Young's modulus of the cell wall, cell geometry). This link is, however, not straightforward. Even for an idealized tissue composed of identical cells of internal turgor P , wall thickness h and size R , dimensional analysis states that the tissue Young's modulus should depend on both the turgor pressure and the cell properties through two independent dimensionless numbers, namely P/E_{wall} and h/R . It is possible to simplify the prediction and derive scaling relations when the turgor pressure is higher than the bending stiffness ($P \gg E_{\text{bending}}$) so that the cell walls are all pre-stretched and in tension. As the liquid is incompressible, it is generally not possible to deform such a tissue without further stretching the walls, unlike the case of an isolated cell

(Figure 1.7e). The tissue's Young's modulus E_{tissue} is then dominated by the stretching mode of deformation, as in the case of the cellular bulk modulus, which gives:

$$E_{\text{tissue}} \sim B_{\text{cell}} \sim \left(\frac{h}{R}\right) E_{\text{wall}} \sim \phi E_{\text{wall}}, \quad (1.36)$$

where $\phi \sim h/R$ is the solid (wall) volume fraction of the tissue.

This scaling law is compatible with values of Young's modulus of turgid tissues $E_{\text{tissue}} \sim 10$ MPa and is valid as long as $E_{\text{bending}} \ll P \ll B_{\text{cell}}$. When the turgor pressure drops to zero, for *e.g.* by plasmolyzing the cells in an osmotic solution, the tissue modulus sharply drops because the cell walls are no longer stretched and can bend easily. In real plant tissue, the situation is complicated by the fact that the cell wall's modulus E_{wall} itself is not constant but strongly varies with the deformation (Figure 1.7c), yielding complex turgor pressure dependences. Note that in all this discussion, we have assumed that the tissue remains always close to full hydration, even when the turgor drops to zero. When the tissue further loses water below the onset of plasmolysis, as during drying in air, the tissue Young's modulus E_{tissue} may rise again because the solid fraction ϕ increases, until it reaches the wall Young's modulus E_{wall} (see the discussion in Chapter 5 in the context of roots). More details on this question from the standpoint of cellular materials can be found in ref. 57, 111 and 163.

1.2.3 Poroelasticity: From Cell to Tissue

So far, we have discussed the elastic behavior of a plant cell and tissue without considering the flow of water within it. However, we have seen that the cell wall and plasma membrane are permeable to water. Therefore, any deformation resulting in a local change in turgor pressure, such as the bending of a stem (Chapter 2) or the squeezing of a fruit, must induce a movement of water within the medium. The same is true for a plant cell or tissue immersed in a solution of different osmolarity. To restore the water potential balance, the tissue must absorb or expel water and therefore must swell or shrink elastically. This coupling between flow and deformation in elastic porous media like plant tissues is described by poroelasticity or poromechanics theory.³⁴ As we shall see, poroelasticity sets the timescale of response of plant tissues to sudden change of water potential, and thus provides a bound for all water-driven movements.^{39,50,146}

1.2.3.1 The Cellular Relaxation Time

We first consider poroelasticity at the cellular level. Consider an isolated plant cell of initial volume V_i immersed in a bath at thermodynamic equilibrium ($\Psi_{\text{bath}} = \Psi_{\text{cell},0} = P_0 - c_0 \mathcal{R}T$), where P_0 is the initial turgor pressure of the cell and c_0 is its initial solute concentration (Figure 1.8a). The water potential balance is suddenly perturbed at time $t=0$, for example by

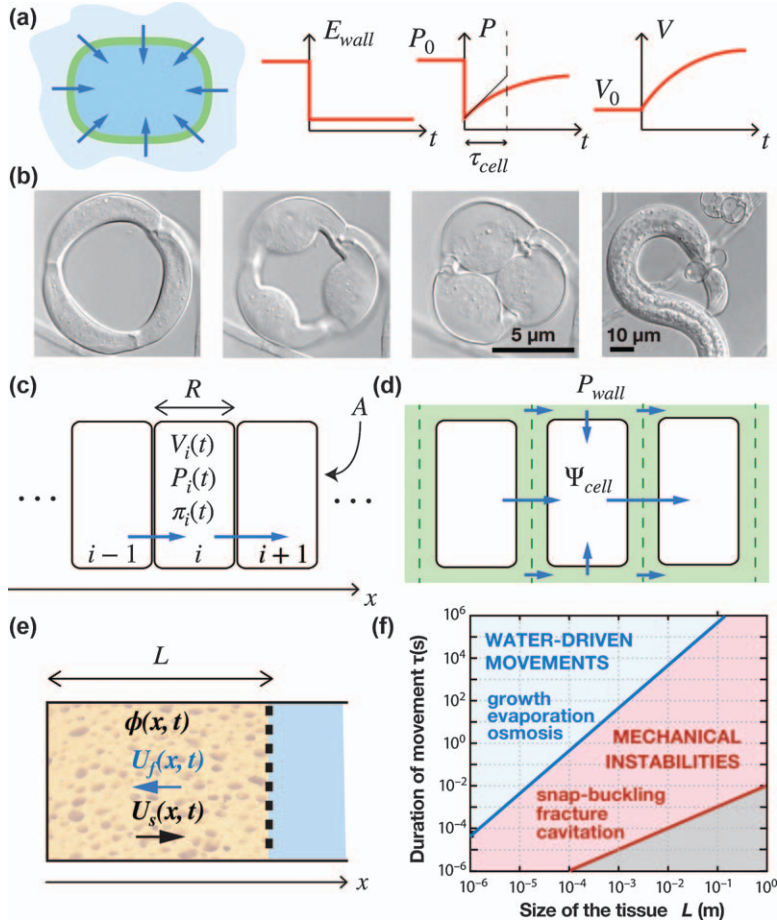


Figure 1.8 Poroelasticity. (a) Cellular relaxation timescale τ_{cell} induced by a sudden change of water potential (here a sudden drop of the cell wall Young's modulus). (b) Rapid swelling of the ring cells of the trap of the carnivorous fungus *Arthrobotrys brochopaga*. Reproduced from ref. 114 with permission from TIB, Copyright 1995. (c) Philip's model of water transport in a one-dimensional tissue (transmembrane transport only). (d) Molz and Ikenberry's model¹⁰⁰ taking into account both the apoplast and transmembrane pathway. (e) Two-fluid continuum model for a poroelastic medium. (f) Physical classification of plant movements showing the poroelastic time $\tau_p \propto L^2$ (blue line) and the inertial time $\tau_{inertia} \sim L\sqrt{\rho/E}$ (red curve), below which no motion is possible.¹⁴⁶

suddenly changing the internal turgor pressure (a similar result holds for a perturbation of solute concentration or external water potential). What is the swelling/shrinking dynamics of the cell in response to this perturbation?

To answer this question, we use mass conservation and state that the change in volume V of the cell per unit time is equal to the flow rate of water

through its surface S . Using eqn (1.13) of the water flux J across an ideal semi-permeable membrane, this gives:

$$\frac{dV}{dt} = -J \times S = -L_p(\Psi_{\text{cell}} - \Psi_{\text{bath}})S = -L_p(P - cRT - \Psi_{\text{bath}})S, \quad (1.37)$$

where L_p is the hydraulic conductivity of the membrane. For small perturbations around the initial state, we can write: $V = V_0 + \delta V(t)$, $S = S_0 + \delta S(t)$, $P = P_0 + \delta P(t)$ and $c = c_0 + \delta c(t)$. Since inertia is negligible, the mechanical equilibrium is always satisfied and we can use the pressure/volume relationship $\delta P = B_{\text{cell}}(\delta V/V_0)$ seen in Section 2.2 (eqn (1.33)). Finally, assuming the conservation of solute during the dynamics implies: $\delta c/c_0 = -\delta V/V_0$. At the lowest order, eqn (1.37) then reduces to a linear relaxation equation for the turgor pressure:

$$\frac{d\delta P}{dt} = -\frac{1}{\tau_{\text{cell}}} \delta P \quad \text{with} \quad \tau_{\text{cell}} = \frac{V_0}{L_p S_0 (B_{\text{cell}} + \Pi)}, \quad (1.38)$$

where τ_{cell} is the cell relaxation time and $\Pi = c_0 RT$ is the osmotic pressure. Generally, $B_{\text{cell}} \gg \Pi$; writing $V/S \sim R$ where R is the typical size of the cell thus gives:

$$\tau_{\text{cell}} \sim \frac{R}{L_p B_{\text{cell}}}. \quad (1.39)$$

The cell relaxation time thus increases when the cell size increases or when the membrane permeability or cell elasticity decreases. Typical measurements in giant algal cells of $R = 200 \mu\text{m}$, $B_{\text{cell}} = 30 \text{ MPa}$, and $L_p = 2 \times 10^{-12} \text{ ms}^{-1} \text{ Pa}$ give $\tau_{\text{cell}} = 3.5 \text{ s}$.

The cell relaxation time sets the shortest response time of a plant cell to a sudden (small) change of water potential: whatever the timescale of other biochemical or genetic processes, *e.g.* ion flux, aquaporin opening, change of wall mechanical properties, a cell cannot change its volume in a time $\tau < \tau_{\text{cell}}$. The cell relaxation time thus defines the fastest possible swelling/shrinking movement at the cellular level.^{39,50} This hydraulic limit is probably reached in some carnivorous fungi (*e.g.* *Arthrobotrys brochopaga*), which have evolved special mycelial structures to capture nematodes¹¹⁵ (Figure 1.8b). In these organisms, the trap consists of a constrictive ring composed of three connected cells of size $R \sim 5 \mu\text{m}$. When a nematode enters the ring, the cells rapidly inflate inward, wrapping the nematode in less than 1/10 of second. The current hypothesis for this rapid movement is that the cell wall of the ring is bi-composite, with a very rigid outer wall surrounding a more flexible inner wall. Upon stimulation, the outer wall suddenly breaks, which is equivalent to a sudden drop in the Young's modulus of the wall. To satisfy mechanical equilibrium and Hooke's law, $[\sigma = (R/2h)P = E_w \varepsilon_{\text{el}}$, see Section 2.2], the turgor must therefore drop

abruptly, resulting in water being sucked in and the cell swelling very rapidly due to its small size ($\tau_{\text{cell}} \propto R$).

1.2.3.2 Water Diffusion in Plant Tissues

We can extend the previous approach to the tissue level. The simplest model of a plant tissue is a one-dimensional chain of identical rectangular cells in which water is transported from cell to cell through the cell plasma membranes, without considering the cell wall between the cells (Philip's model,¹²² see Figure 1.8c). Using the water transport law (eqn (1.13)), the mass conservation for the volume V_i of the cell i is given by (assuming $\Psi_{\text{bath}} = 0$):

$$\frac{dV_i}{dt} = AL'_p(P_{i+1} - \Pi_{i+1} - P_i + \Pi_i) - AL'_p(P_i - \Pi_i - P_{i-1} + \Pi_{i-1}), \quad (1.40)$$

where A is the cell area in the direction of the flow, $L'_p = L_p/2$ is the effective membrane hydraulic conductivity (the factor $1/2$ comes from the fact that two cell membranes has to be crossed per cell), P_i is the turgor pressure of cell i and $\Pi_i = c_i RT$ is the osmotic pressure of the cell i . Using again the small perturbation approximation and the initial water potential equilibrium condition, eqn (1.40) reduces to:

$$\frac{d\delta P_i}{dt} = \frac{1}{\tau_{\text{cell}}} (\delta P_{i+1} + \delta P_{i-1} - 2\delta P_i). \quad (1.41)$$

where $\tau_{\text{cell}} = V_0/[AL'_p(B_{\text{cell}} + \Pi)]$ is the single cell relaxation time. Using the continuum approximation : $\delta P_i(t) \rightarrow \delta P(x, t)$, the set of discrete differential eqn (1.41) becomes a single partial differential equation:

$$\frac{\partial \delta P}{\partial t} = \left(\frac{R^2}{\tau_{\text{cell}}} \right) \frac{\partial^2 \delta P}{\partial x^2} = \mathcal{D}_{\text{Philip}} \frac{\partial^2 \delta P}{\partial x^2}, \quad (1.42)$$

with $\mathcal{D}_{\text{Philip}} = R^2/\tau_{\text{cell}} \sim RL_p B_{\text{cell}}$.

Eqn (1.42) corresponds to a diffusion equation for the relaxation of the turgor pressure, with a diffusion coefficient $\mathcal{D}_{\text{Philip}}$. The characteristic time for water transport through a tissue of length L , called the *poroelastic time* τ_p , is given by:

$$\tau_p \sim \frac{L^2}{\mathcal{D}_{\text{Philip}}} \sim \left(\frac{L}{R} \right)^2 \tau_{\text{cell}} \sim \frac{L^2}{RL_p B_{\text{cell}}}. \quad (1.43)$$

The poroelastic time τ_p depends on the cellular hydraulic and mechanical properties and scales with the tissue size as $\propto L^2$.

The Philip's model has been extended to take into account both the cell-to-cell pathway and the apoplast pathway, *i.e.* through the cell wall (see Box 1.1) by Molz and Ikenberry¹⁰⁰ (Figure 1.8d). This model assumes that water can

be transported from cell to cell by a gradient of cell water potential Ψ_{cell} , and into the wall by a gradient of hydrostatic pressure P_{wall} . Water can also be exchanged perpendicularly between the wall and the cells. In this framework, the water transport is described by two diffusion equations with a coupling term:

$$\begin{aligned}\frac{\partial \Psi_{\text{cell}}}{\partial t} &= D_1 \frac{\partial^2 \Psi_{\text{cell}}}{\partial x^2} - C_1 (\Psi_{\text{cell}} - P_{\text{wall}}) \\ \frac{\partial P_{\text{wall}}}{\partial t} &= D_2 \frac{\partial^2 P_{\text{wall}}}{\partial x^2} + C_2 (\Psi_{\text{cell}} - P_{\text{wall}})\end{aligned}\quad (1.44)$$

where $D_1 = D_{\text{Philip}}$ and $D_2 = 2B_{\text{wall}}k_{\text{wall}}/2\eta$ is a water diffusion coefficient in the cell wall, with B_{wall} the wall bulk modulus, k_w the cell wall (Darcy) permeability and η the water viscosity. The coupling terms involve the properties of the cell wall and cell membrane: $C_1 = 6AL_p(B_{\text{cell}} + \Pi)/V_0$ and $C_2 = 6L_pB_{\text{wall}}/\phi R$, where $\phi \ll 1$ is the wall volume fraction.

In practice, water diffuses much faster through the wall than from cell to cell, because the wall is much more rigid than the cell ($D_2 \approx 100 D_1$). However, the small solid fraction of the wall and the large exchange surface between wall and cells make the coupling between the two paths very strong. In this situation, it can be shown that there is a local quasi-equilibrium between the water potential of the wall and the water potential of the adjacent cell, such that $\Psi_{\text{cell}} \approx P_{\text{wall}} = \Psi_{\text{tissue}}$, where Ψ_{tissue} is the water potential of the tissue. The two coupled equations can then be reduced into a single effective diffusion equation for water transport:

$$\frac{\partial \Psi_{\text{tissue}}}{\partial t} = D_{\text{tissue}} \frac{\partial^2 \Psi_{\text{tissue}}}{\partial x^2}, \quad (1.45)$$

where D_{tissue} is an effective water diffusion coefficient given by:

$$D_{\text{tissue}} = \frac{D_1 C_2 + D_2 C_1}{C_1 + C_2}. \quad (1.46)$$

Typical values for plant tissues (taking $R \sim 10/100 \mu\text{m}$, $L_p \sim 10^{-12} \text{ ms}^{-1} \text{ Pa}^{-1}$, $B_{\text{cell}} \sim 10 \text{ MPa}$, $\phi \sim 0.1$, $B_{\text{wall}} \sim 100 \text{ MPa}$, $k_{\text{wall}} \sim 10^{-18} \text{ m}^2$) gives $D_{\text{tissue}} \sim 10^{-9} - 10^{-10} \text{ m}^2 \text{ s}^{-1}$, in agreement with measurements.^{100,148} A three-dimensional extension of this model, taking into account the transport in vascularized tissues, can be found in ref. 130 and 131.

1.2.3.3 Poroelasticity in Continuum Media

When the effective medium approximation is valid, one can approach water diffusion in plant tissues using continuum equations and the theory of poroelasticity (see for *e.g.* ref. 34). We derive here a simple one-dimensional poroelastic model for a porous material made of an incompressible solid matrix of volume fraction $\phi = \delta V_s / \delta V$, where δV_s is the

local volume of solid and δV the local total volume, infiltrated by an incompressible liquid of volume fraction $\phi_f = \delta V_f / \delta V = 1 - \phi$, where δV_f is the local volume of fluid (Figure 1.8e). We note $U_s = (1/\delta V_s) \int_{\delta V_s} d\tau U_s^{\text{local}}$ (resp. $U_f = (1/\delta V_f) \int_{\delta V_f} d\tau U_f^{\text{local}}$) the volume averaged velocity of the solid matrix (resp. fluid). The conservation of mass written for the total medium (solid and fluid) and for the solid phase gives two equations:

$$\begin{aligned} \frac{\partial}{\partial x} (\phi U_s + (1 - \phi) U_f) &= 0, \\ \frac{\partial \phi}{\partial t} + \frac{\partial \phi U_s}{\partial x} &= 0. \end{aligned} \quad (1.47)$$

Neglecting fluid and solid's inertia, the conservation of momentum for the total medium and for the fluid phase gives:

$$\begin{aligned} \frac{\partial}{\partial x} (\sigma_s - P) &= 0, \\ J \equiv (1 - \phi)(U_f - U_s) &= -\frac{k(\phi)}{\eta} \frac{\partial P}{\partial x}. \end{aligned} \quad (1.48)$$

Here, σ_s is the volume-averaged stress in the solid matrix corrected by a fluid pressure term: $\sigma_s = (1/\delta V) \int_{\delta V_s} d\tau \sigma_s^{\text{local}} + \phi P$, where P is the pressure in the fluid phase (minus the atmospheric pressure by convention). This definition of the solid stress, also called Terzaghi effective stress, ensures that the solid stress is zero when the matrix is immersed in a fluid of uniform pressure without deformation. The second equation for the fluid's momentum balance is Darcy's law, where J is the volume flux of fluid, k is the Darcy permeability of the porous medium and η is the fluid's viscosity.

The system is closed by adding a constitutive law for the mechanical behavior of the solid phase. Assuming an elastic linear relationship between stress and deformation (Hooke's law), we can write:

$$\sigma_s = E \left(\frac{\phi_0 - \phi}{\phi_0} \right), \quad (1.49)$$

where ϕ_0 is the solid fraction of the undeformed matrix, $(\phi_0 - \phi)/\phi_0$ is the one-dimensional elastic strain and $E = -\phi(d\sigma_s/d\phi)$ is a one-dimensional Young's modulus of the solid matrix.

Linearizing eqn (1.47)–(1.49) around the rest state $P = 0$, $U_s = U_f = 0$ and $\phi = \phi_0$ gives:

$$\frac{\partial \phi}{\partial t} = \mathcal{D} \frac{\partial^2 \phi}{\partial x^2} \quad \text{with} \quad \mathcal{D} = \frac{kE}{\eta}. \quad (1.50)$$

One recovers a diffusion equation for the transport of water in the poro-elastic medium, as obtained previously using a discrete description of the plant tissue. The effective diffusion coefficient \mathcal{D} is a function of the fluid's

viscosity η , the Darcy permeability k and the elastic Young's modulus E of the porous matrix. The poroelastic time of water diffusion across a tissue of size L is given by:

$$\tau_p = \frac{L^2}{D} = \frac{\eta L^2}{kE}. \quad (1.51)$$

As for the cell relaxation time at the cell scale, the poroelastic time τ_p provides a bound for the fastest possible water-driven movements in plants at the tissue and organ level.¹⁴⁶ A plant motion occurring on a timescale $\tau > \tau_p$ can rely on water transport, whereas systems with $\tau < \tau_p$ must use other mechanisms (Figure 1.8f). The strong size dependence of the poroelastic time ($\tau_p \propto L^2$) shows that hydraulic movements are increasingly less efficient in terms of speed as the system size increases. We shall see in Section 2.5 how the use of mechanical instabilities enables plants to overcome this hydraulic limit.

1.2.4 Growth

So far, we have dealt with the small deformation regime of plant tissues, where strains are mainly reversible. We now address the opposite extreme deformation regime corresponding to plant growth. Growth is the irreversible and sustained expansion of cells under physiological conditions.¹⁵⁵ It is obviously a very complex phenomenon that requires a continuous interplay between biochemistry, mechanics and hydraulics to maintain homeostasis. During growth, the cell wall must be continuously synthesized while it expands in order to maintain its mechanical and structural integrity. At the same time, the absorption of water from the surrounding environment must be precisely balanced, in order to allow the increase in cell volume and thus the expansion.

The concept of growth usually encompasses cell division, cell differentiation and the actual growth of cells, *i.e.* their increase in size. Cell division occurs in localized regions called meristems. In plants, a distinction is made between primary growth, responsible for the elongation of organs, and secondary growth, responsible for the radial thickening of organs. Primary growth is driven by meristems located at the tip (apex) of stems and roots, and therefore called apical meristems. The meristem of secondary growth is the cambium, a ring of cells around the axis of stems and roots. We focus here mainly on primary growth and on the mechanical aspects of cell expansion, leaving aside the question of cell division and differentiation. A discussion of growth from a modeling perspective is found in Chapter 4.

1.2.4.1 Cell Wall Rheology: The Lockhart–Ortega Model

The basic mechanics of plant growth have been revealed by seminal experiments conducted on giant algal cells.^{60,125–127} First, growth requires the existence of a minimum turgor pressure to occur, *i.e.* a minimum stretch or

Box 1.4 Extension of poroelasticity to hygroscopic media.

We have seen how the coupling between flow (Darcy's law) and elastic deformation (Hooke's law) yields a diffusion equation for the transport of water in a deformable porous medium. Similar fluid–solid couplings occur in hygroscopic media like hydrogels, except that in the latter case the strong chemical affinity between the water and the polymer chains generates an additional osmotic driving force for the transport of water. Hydrogels provide a simple model for the hygroscopic behavior of the plant cell wall. We give below a one-dimensional version of the theory developed by Bertrand *et al.* to describe the swelling dynamics of ideal elastomeric gels.¹²

As in a classical poroelastic medium, the total stress in the gel can be written as the sum of a solid stress σ_s and a fluid (pore) pressure P :

$$\sigma = \sigma_s - P. \quad (1.52)$$

For a gel the solid stress is of entropic origin and represents the elastic stretching stress of the polymer chains network (as before, the isotropic atmospheric pressure has been removed from the definition of P and σ , such that for a gel at atmospheric pressure: $P = 0$ and $\sigma = 0$). This elastic contribution for uniaxial deformation can be written as:¹²

$$\sigma_s^{1D} = \frac{\mathcal{R}T}{v_p} \left(\frac{1 - \phi^2}{\phi} \right), \quad (1.53)$$

where ϕ is the local volume fraction of solid and v_p is the molar volume of polymers in the dry state. Note that with this convention, the elastic stress is null when the gel is dry ($\phi = 1$, no water inside).

For an ideal elastomeric hydrogels, it is possible to decompose the matrix potential (the water potential inside the gel) between a pressure term and an osmotic term, by analogy with dilute solutions (see ref. 12):

$$\Psi_{\text{gel}} = P + \Psi_{\text{os}}. \quad (1.54)$$

The osmotic term is the derivative of the mixing Helmholtz free energy of the gel per unit volume, with respect to change of volume. It can be obtained from the Flory–Huggins theory of polymer solutions as:

$$\Psi_{\text{os}} = \frac{\mathcal{R}T}{v_w} \left(\phi + \ln(1 - \phi) - \frac{\phi}{\alpha} + \chi\phi^2 \right), \quad (1.55)$$

where v_w is the molar volume of pure water in the reference state. The first three terms in brackets reflect the entropy of mixing, where α is a measure of the volume per polymer molecule relative to the volume per fluid molecule in the mixture. The fourth term reflects the enthalpy of mixing,

where χ is a dimensionless interaction parameter.¹² Once the water potential is known, the generalized Darcy's law is given by:

$$J \equiv (1 - \phi)(U_f - U_s) = -\frac{k(\phi)}{\eta} \frac{\partial \Psi_{\text{gel}}}{\partial z}. \quad (1.56)$$

By combining eqn (1.53)–(1.56) with the mass conservation (1.47), and linearizing around a rest state, we recover a similar diffusion equation for the evolution of ϕ as derived previously (eqn (1.50)), except that the diffusion coefficient now incorporates the osmotic contribution:

$$\mathcal{D}_{\text{gel}} = \frac{kE_{\text{gel}}}{\eta} \quad \text{with} \quad E_{\text{gel}} = -\phi \frac{d(\sigma_s^{1D} + \Psi_{\text{os}})}{d\phi}. \quad (1.57)$$

We can apply this theory to estimate the swelling of a “water bead” initially in the dry state with a radius R_{dry} , and immersed in a bath of pure water at atmospheric pressure where it reaches an equilibrium radius R_{eq} . In this situation, swelling occurs in three dimensions, but the above one-dimensional model can be applied to each direction independently, by symmetry of the problem. At thermodynamic equilibrium, the water potential of the gel is equal to that of the bath, such that: $\Psi_{\text{gel}}(\phi_{\text{eq}}) = P + \Psi_{\text{os}}(\phi_{\text{eq}}) = 0$. To be consistent with the one-dimensional theory, ϕ_{eq} must be understood as the *linear* solid fraction, not the volume solid fraction, *i.e.* $\phi_{\text{eq}} = \phi_{\text{dry}} \times (R_{\text{eq}}/R_{\text{dry}})$ with $\phi_{\text{dry}} = 1$. On the other hand, mechanical equilibrium implies that the total stress is null (the bath is at atmospheric pressure), such that: $\sigma^{1D}(\phi_{\text{eq}}) - P = 0$. The linear solid fraction of the water bead at equilibrium thus satisfies:

$$\frac{\mathcal{R}T}{v_p} \left(\frac{1 - \phi_{\text{eq}}^2}{\phi_{\text{eq}}} \right) + \frac{\mathcal{R}T}{v_w} \left(\phi_{\text{eq}} + \ln(1 - \phi_{\text{eq}}) - \frac{\phi_{\text{eq}}}{\alpha} + \chi \phi_{\text{eq}}^2 \right) = 0. \quad (1.58)$$

In practice, ϕ_{eq} is small and $v_p/(\alpha v_w) \gg 1$. At the lowest order, the swelling ratio is thus given by:

$$\frac{R_{\text{final}}}{R_{\text{dry}}} = \frac{\phi_{\text{dry}} = 1}{\phi_{\text{eq}}} \approx \sqrt{\frac{v_p}{\alpha v_w}} \approx 6, \quad (1.59)$$

with typical values for hydrogels: $\alpha \approx 250$ and $v_w/(\alpha v_p) \approx 10^{-4}$ (see ref. 12).

stress for the cell wall to yield. Second, above this yield pressure, the rate of cell expansion, or growth rate, depends on the pressure difference between the turgor pressure and the yield pressure. Third, when applying increments of turgor pressure, the growth rate stabilizes at its steady value only after a given relaxation time.

These observations are reminiscent of the behavior of yield-stress fluids in soft matter, such as emulsions, polymeric gels or clays, which exhibit elastic behavior below a yield-stress and viscous behavior above.⁶ From the mechanical standpoint, the simplest constitutive law of the plant cell wall is therefore that of a Bingham fluid or an elasto-viscoplastic fluid. Such Bingham model was first proposed by Lockhart in 1965⁹² and then extended by Ortega in 1985¹¹⁹ to take into account elasticity. For uniaxial deformation, the Lockhart–Ortega rheology of the cell wall can be written as:

$$\sigma_{\text{wall}} = E_{\text{wall}}\varepsilon_{\text{el}} \quad \text{and} \quad \varepsilon = \varepsilon_{\text{el}} + \varepsilon_{\text{ir}},$$

$$\text{with} \quad \begin{cases} \dot{\varepsilon}_{\text{ir}} = 0 & \text{if } \sigma_{\text{wall}} < \sigma_Y, \\ \dot{\varepsilon}_{\text{ir}} = \Phi_{\text{wall}}(\sigma_{\text{wall}} - \sigma_Y) & \text{if } \sigma_{\text{wall}} > \sigma_Y. \end{cases} \quad (1.60)$$

In this model, the total strain in the cell wall ε is decomposed into an elastic part, ε_{el} , and an irreversible or plastic part, ε_{ir} , which represents growth (Figure 1.9a). Below a critical stress σ_Y , the cell wall behaves as an elastic solid ($\varepsilon = \varepsilon_{\text{el}}$) and follows Hooke's law with a Young's modulus E_{wall} . Above σ_Y , the cell wall deforms irreversibly and flows with a strain rate $\dot{\varepsilon}_{\text{ir}}$ proportional to the excess stress ($\sigma_{\text{wall}} - \sigma_Y$). The proportionality coefficient Φ_{wall} between the strain rate and the excess stress is called the extensibility of the cell wall and is associated with the irreversible creep of the wall under stress, also called wall-loosening.¹⁶⁶ Dimensionally, the cell wall extensibility is an inverse viscosity [unit (Pa s)⁻¹]. However, it should be kept in mind that the extensibility reflects a complex process at the microscopic level, including the addition of mass and a chemically mediated remodeling of wall material. The extensibility strongly depends on the temperature – a sign that it is under the control of cell metabolism¹²⁷ – and can be modified under the action of pH-dependent wall-loosening enzymes, such as expansins.^{25,32} Several molecular-scale^{2,42,132,167} or thermodynamic⁷ models have been proposed to describe this active process, some of which recovering a Bingham-like rheology at the macroscopic level (see Chapter 4 for a detailed presentation of one of these microscopic models).

The simple uniaxial Lockhart–Ortega model (1.60) has been extended to anisotropic cell wall under multiaxial stress, either by assuming an anisotropic extensibility⁴⁰ or an anisotropic elasticity by analogy with fiber-reinforced composite materials.^{15,18} A more complex constitutive law explicitly accounting for the reorientation of microfibrils under flow has been also developed, by analogy with liquid crystals.⁴³ For such tensorial laws, the question of whether the cell wall yields above a critical strain ε_Y or a critical stress σ_Y , which is equivalent in the one-dimensional Lockhart model, is of importance, as the principal direction of strain may not coincide with the principal direction of stress.¹¹⁷ For elongated cells and organs for which $\sigma_{\perp} > \sigma_{\parallel}$ (see Section 1.2.1), the direction of growth is mainly longitudinal and thus perpendicular to the maximal stress, suggesting that the yield condition in terms of strain is more relevant.

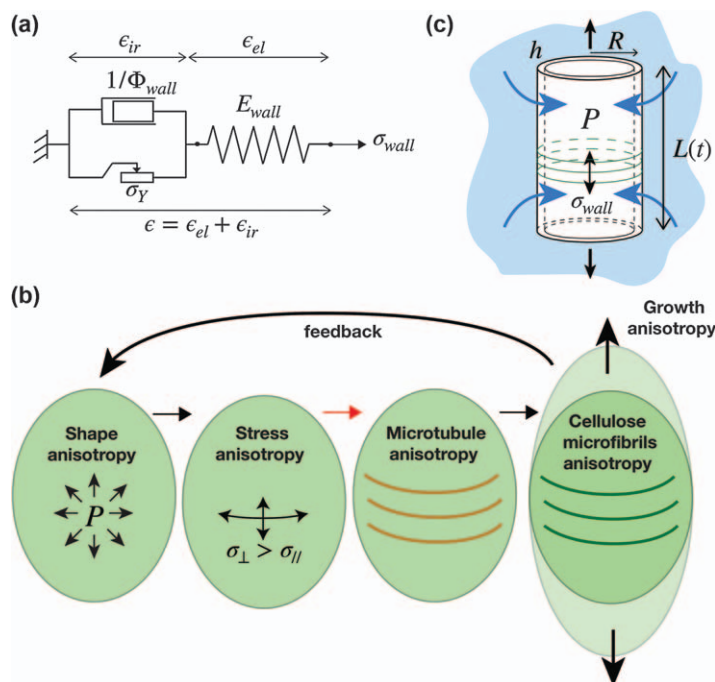


Figure 1.9 Growth and cell wall rheology. (a) One-dimensional mechanical representation of the elasto-viscoplastic rheology of the cell wall. (b) Mechanosensing (red arrow) of the wall stress by the cortical microtubules (brown) fixing the orientation of cellulose microfibrils (green) generates a mechanical feedback loop between shape and growth. (c) Unidirectional growth of a single cell immersed in a water bath (Lockhart's model).

Finally, a growing body of evidence suggests that the cell wall rheology is regulated not only by molecular signals, but also by the mechanical state of the wall itself.¹⁵⁹ A key molecular actor of this feedback is the cortical microtubules, whose orientation determines the orientation of the cellulose microfibrils in the wall, and thus wall anisotropy (see Box 1.1. and Figure 1.1b). Experiments show that the orientation of the microtubules aligns with the direction of maximal stress in the wall, generating a feedback loop between the organ's shape (determining stress direction) and material anisotropy (determining growth direction and thus shape)⁶³ (Figure 1.9b). This mechanical feedback is taken into account in the most recent rheological models¹¹⁸ but the precise transduction mechanism is still debated.^{64,117} More generally, how mechanics modified growth, either through direct effect on the wall stress or through the perception and transduction of internal and external mechanical signals – a process known as thigmomorphogenesis – is a very active area of research in plant biophysics. A discussion of these aspects in the context of root growth is given in Chapter 5.

1.2.4.2 Growth of a Single Plant Cell

The Lockhart–Ortega rheology can be used to describe the unidirectional and uniform steady growth of an isolated cell, modeled as a cylinder of fixed radius R and length $L(t)$, immersed in an external bath of water potential Ψ_{bath} (Figure 1.9c). This situation typically corresponds to the growth of the giant internode cells of the green algae *Chara* or *Nitella*. For these cells, the wall expansion is evenly distributed over the wall surface and growth is uniform along the cell, a mode of growth called diffuse growth^{§§}. Moreover, the cellulose microfibrils in these cells run mainly circumferentially, restricting growth in the radial direction and promoting growth in length.

In this cylindrical geometry, the balance between the turgor pressure and the wall stress implies that the longitudinal wall stress is given by $\sigma_{\text{wall}} = PR/(2h)$, where h is the wall thickness and P the turgor pressure. For a steady state of growth the elastic strain ε_{el} is constant. The growth strain rate, also termed relative elongation rate (RER) or relative elementary growth rate (REGR) in the plant science community, is then given by $\dot{\varepsilon} = \dot{\varepsilon}_{\text{ir}} = (1/L)(dL/dt)$. Combining the force balance and the Lockhart–Ortega wall rheology (1.60) thus implies:

$$\frac{1}{L} \frac{dL}{dt} = \Phi(P - P_Y), \quad (1.61)$$

where $\Phi = (\Phi_{\text{wall}}R/2h)$ is an effective extensibility defined at the cellular level and $P_Y = 2h\sigma_Y/R$ is the yield turgor pressure for growth. This first Lockhart's equation must be complemented by a second equation for water transport. Indeed, for cell expansion to be possible, an inward flow of water must compensate for the increase in volume, which requires a difference in water potential between the inside and outside of the cell. Using the water transport eqn (1.13), the second Lockhart equation is:

$$\frac{dL}{dt} = -\frac{2L}{R} L_p (P - c\mathcal{R}T - \Psi_{\text{bath}}), \quad (1.62)$$

where L_p is the hydraulic conductivity of the membrane and c the cell solute concentration. To close the system, a third Lockhart equation should be added to describe the temporal evolution of the solute concentration.¹⁰⁵ We assume here that growth is slow enough that osmotic balance is maintained, so that solute concentration remains constant. The solution of (1.61–1.62) is therefore:

$$\frac{1}{L} \frac{dL}{dt} = \frac{2L_p}{R} \frac{c\mathcal{R}T - P_Y}{1 + \frac{2L_p}{R\Phi}} \quad \text{and} \quad P = \frac{P_Y + \frac{2L_p}{R\Phi} c\mathcal{R}T}{1 + \frac{2L_p}{R\Phi}}. \quad (1.63)$$

^{§§}Diffuse growth is opposed to tip growth, characterized by a highly localized wall expansion at the tip of the cells. Tip growth is the mode of growth of invading cells like root hairs or pollen tubes and is discussed in Chapter 7.

Two limiting regimes can be considered depending on the value of the Lockhart's parameter: $\mathcal{L} = 2L_p/R\Phi$. For $\mathcal{L} \gg 1$ (small extensibility, large membrane permeability), eqn (1.63) becomes:

$$\frac{1}{L} \frac{dL}{dt} \approx \Phi(cRT - P_Y) \quad \text{and} \quad P \approx cRT. \quad (1.64)$$

This regime is called the extensibility-limited regime. In this case the growth rate of the cell is set by how fast the cell can extend its cell wall (embedded in the parameter Φ), not by its ability to take up water across the plasma membrane. The water potential balance is then almost satisfied and the turgor pressure is simply given by the osmotic pressure cRT . Growth of most plant organs is assumed to operate in this extensibility-limited regime. From typical growth rate in young shoots $\dot{\epsilon} \sim 0.1 - 1 \text{ h}^{-1}$ (see ref. 144) and using standard values $cRT \sim 0.5 \text{ MPa}$, $P_Y \sim 0.3 \text{ MPa}$ ³¹ and $R/2h \sim 10$, we find that the cell wall “viscosity” is $1/\Phi_{\text{wall}} \sim 10\text{--}100 \text{ GPas}$ – a value close to the viscosity of ice!⁵⁴

For the opposite regime $\mathcal{L} \ll 1$ (large extensibility, small membrane permeability), the Lockhart eqn (1.63) becomes:

$$\frac{1}{L} \frac{dL}{dt} \approx \frac{2L_p}{R} (cRT - P_Y) \quad \text{and} \quad P \approx P_Y. \quad (1.65)$$

In this conductivity-limited regime, the extensibility of the cell is so large that the growth rate is limited, not by the cell-wall extensibility, but by the water uptake resistance set by the plasma membrane. The turgor pressure is then poised at the yield pressure P_Y , not at the osmotic pressure cRT , meaning that a significant water potential gradient exists between the inside and outside of the cell.

1.2.4.3 Extension of Lockhart's Model to Tissues

Since the pioneering work of Molz and Boyer,⁹⁹ the Lockhart equations have been extended to multicellular tissues using cell-based models to couple water transport and growth.²⁶ A scaling analysis of the problem can also be made using the same kind of continuum approach as we used for poroelasticity (Section 2.3). Consider a tissue of size L growing at a constant rate $\dot{\epsilon}$. Volume conservation requires a water flux to sustain growth, which is given by: $J = (1/S)dV/dt = \dot{\epsilon}L$, where V is the volume of the growing tissue and S the cross-section perpendicular to the flow. From Darcy's law, this water flux must be induced by a turgor pressure gradient across the tissue (assuming uniform solute concentration) given by: $(\Delta P/L) = (\eta/k)J \sim (\eta/k)\dot{\epsilon}L$, such that:

$$\dot{\epsilon} \sim \frac{k \Delta P}{\eta L^2}. \quad (1.66)$$

This relationship is the tissue version of the second Lockhart equation (1.62) on water transport. On the other hand, the force balance between the internal turgor pressure and the cell wall still holds at the tissue level, such that $\sigma \sim (R/h)P$. Using the Lockhart–Ortega rheology for the wall in steady state, we recover the same relationship as the first Lockhart's equation:

$$\dot{\epsilon} \sim \Phi(P - P_Y). \quad (1.67)$$

This analysis shows that the gradient of turgor pressure induced by tissue growth is negligible if $\Delta P \ll P - P_Y$, which using eqn (1.66) gives:

$$\mathcal{L}_{\text{tissue}} = \frac{k}{\Phi \eta L^2} \gg 1. \quad (1.68)$$

The dimensionless number $\mathcal{L}_{\text{tissue}}$ is the tissue equivalent of the Lockhart number \mathcal{L} defined at the cellular level. For $\mathcal{L}_{\text{tissue}} \gg 1$, the tissue growth rate is limited by cell-wall extensibility while for $\mathcal{L}_{\text{tissue}} \ll 1$, it is limited by water conductivity. Interestingly, this “tissue Lockhart number” depends not only on the mechanics and hydraulic properties of the tissue but also on the system size, with a strong size dependence $\mathcal{L}_{\text{tissue}} \propto L^{-2}$. It has long been assumed that growth in plants operates in the extensibility-limited regime and that growth-associated water potential gradients were small, with the exception of fast-growing tissues such as coleoptiles or roots.^{16,17,30,31,99,148} However, recent measurements of turgor pressure at cellular resolution in the shoot apical meristem of *Arabidopsis* revealed high cell-to-cell pressure heterogeneity, which can only be predicted by taken into account water transport in addition to wall mechanics.⁹³ Water conductivity was also shown to strongly influence the emergence of lateral roots in *Arabidopsis*.¹²¹ Therefore, the role of water conductivity in the control of growth and development might be more important than previously anticipated, even at small scales.

1.2.4.4 Differential Growth in Rod-like Organs: Plant Tropisms

In the previous section, we considered uniform and unidirectional growth. When growth varies spatially, kinematic constraints may lead to a change in growth direction and thus in organ shape. We consider here the important case of differential growth in a slender, rod-like body, such as a plant shoot or stem, which leads to the bending of the organ.^{9,105,144}

To address this question, we model the shoot by a thin rod of length $L(t)$ and constant radius $R \ll L$, restricting its shape to a curve in two dimensions for simplicity. The spatio-temporal shape of the rod is then fully described by the angle $\theta(s, t)$ made by the rod with the vertical axis, where s is the arc length from the fixed base and t is time (Figure 1.10a). By definition, the local curvature of the rod is: $C(s, t) = -\partial\theta/\partial s$. Here the convention is such that curvature is positive when the shoot angle decreases

away from the base, as in Figure 1.10a. The growth kinematics are characterized by the velocity field $v(s, t)$ of the different material points along the rod. A portion ds of the rod at position s and time t increases to a length $(1 + \dot{\epsilon} dt)ds$ at time $t + dt$, where $\dot{\epsilon} = \partial v / \partial s$ is the local growth rate. Similarly, the Lagrangian change of curvature during dt , *i.e.* following the material displacement, is:

$$\frac{dC}{dt} = \frac{\partial C}{\partial t} + v(s, t) \frac{\partial C}{\partial s}. \quad (1.69)$$

We now assume that the growth rate not only varies along the rod but also across the thickness of the rod, from a value $\dot{\epsilon}_2$ at the bottom side of the rod to a value $\dot{\epsilon}_1 < \dot{\epsilon}_2$ at the upper side (Figure 1.10a). During dt , the lower side length thus expands to $(1 + \dot{\epsilon}_2 dt)ds$ while the upper side expands to $(1 + \dot{\epsilon}_1 dt)ds$. As shown in Figure 1.10a, this differential expansion must induce a small change of rod curvature dC . Geometry imposes that: $[(1 + \dot{\epsilon}_2 dt)ds]/(r + R) = [(1 + \dot{\epsilon}_1 dt)ds]/(r - R)$, where $r = (1/dC) \gg R$. At first order, the curvature change induced by differential growth is then given by:

$$R \frac{dC}{dt} \approx \frac{\dot{\epsilon}_2 - \dot{\epsilon}_1}{2}. \quad (1.70)$$

Combining this kinematic growth relation with the expression (1.69) of the Lagrangian derivative gives:

$$R \frac{dC}{dt} = R \left(\frac{\partial C}{\partial t} + v(s, t) \frac{\partial C}{\partial s} \right) = \dot{\epsilon} \Delta, \quad (1.71)$$

with $\Delta = \frac{\dot{\epsilon}_2 - \dot{\epsilon}_1}{\dot{\epsilon}_1 + \dot{\epsilon}_2}$ and $\dot{\epsilon} = \frac{\dot{\epsilon}_1 + \dot{\epsilon}_2}{2}$.

This equation shows that change of curvature in a thin elongated organ is driven by differential growth, here expressed in terms of the relative growth asymmetry $\Delta = (\dot{\epsilon}_2 - \dot{\epsilon}_1)/(\dot{\epsilon}_2 + \dot{\epsilon}_1)$. For a given Δ , the rate of change of curvature is set by the mean growth rate $\dot{\epsilon} = (\dot{\epsilon}_2 + \dot{\epsilon}_1)/2 = \partial v(s, t) / \partial s$. Note that local change in curvature impacts the entire organ orientation because the relationship between angle and curvature is non-local:

$$\theta(s, t) = - \int_0^s C(s', t) ds' + \theta_0. \quad (1.72)$$

where θ_0 is the angle of the shoot at the base.

Eqn (1.71) shows that maintaining a steady curved shape in a growing organ ($\partial C / \partial t = 0$) requires a subtle spatio-temporal regulation of differential growth to satisfy: $v(s, t) R (\partial C / \partial s) = \dot{\epsilon}(s, t) \Delta(s, t)$ – an idea first put forward by Wendy Silk (see ref. 145). Such steady growing shapes are found in many seedlings¹⁴⁵ and also in some compound leaves.¹²⁹ In these examples, the

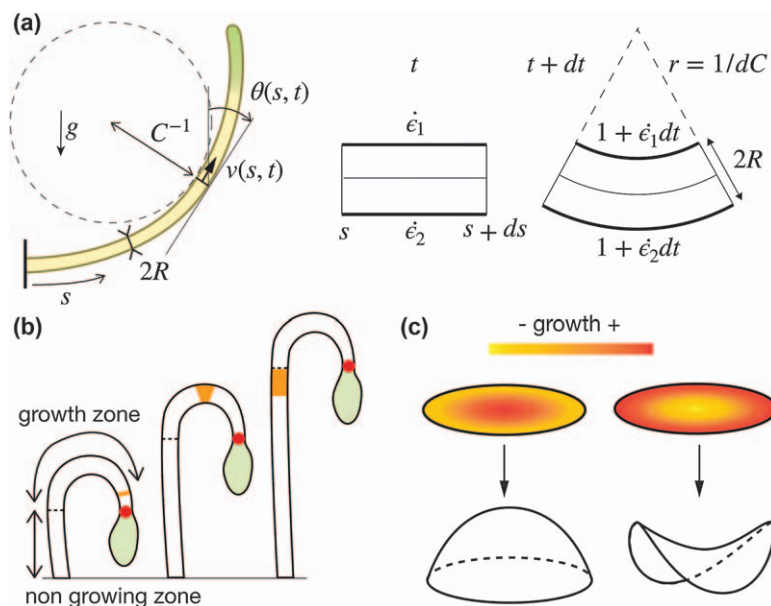


Figure 1.10 Differential growth in slender organs. (a) Kinematic description of a growing rod-like organ and bending induced by differential growth across the thickness. (b) Steady hook shape in a growing shoot, showing the growth and spatio-temporal path of a group of cells (orange region) produced at the apical meristem (red spot) and advected outside the growth zone. (c) Differential growth on a two-dimensional, leaf-like organ induces the generation of a positive (left) or a negative (right) Gauss curvature depending on the growth gradient.

end of the shoot or stem exhibits a hook shape that remains steady and at a fixed distance from the plant apex, all along the growth. Although the hook shape appears steady, each tissue element must follow a complex bending and unbending growth pattern as it moves from the tip, in order to comply with kinematics (see Figure 1.10b).

Bending induced by differential growth is also the basis of most tropic movements in plants,⁵⁸ *i.e.* the directed motion in response to external stimuli such as light (phototropism), touch (thigmotropism) or gravity (gravitropism), which we discuss below. Plants detect gravity using specialized cells (called statocytes), in which starch-rich particles (called amyloplasts or statoliths) sediment under gravity to form miniature “granular” piles at the bottom of the cell^{101,103,109,158} (see Figure 1.11 and Box 1.5). When the cell is inclined, the statoliths move toward the side of the cell even at a small inclination, unlike sand grains, because statoliths are fluidized by the cytoskeleton’s activity (see ref. 13 and Box 1.5). The resulting asymmetric position of statoliths within the cell triggers a complex molecular pathway, leading to the generation of a growth-hormone gradient across the thickness

(the growth hormone in plants is called auxin) and thus to differential growth and organ curvature.

The gravitropic response of plant shoots is inclination-dependent and follows a sine-like shape, such that:

$$\Delta_{\text{gravity}} = \left(\frac{\dot{\epsilon}_2 - \dot{\epsilon}_1}{\dot{\epsilon}_1 - \dot{\epsilon}_2} \right)_{\text{gravity}} = \beta \sin \theta, \quad (1.73)$$

where β is a dimensionless parameter characterizing the gravitropic sensitivity of the plant. This sine-law has classically been interpreted as the consequence of a force-sensing mechanism at the cellular level, the projection of the weight of the statoliths along the side of the cell being proportional to $\sin \theta$. However, recent experiments have shown that the response is independent of the gravity intensity^[4], suggesting that the gravitropic stimulus is the position of the statoliths within the cell, not their weight.^{24,124}

Surprisingly, when the expression (1.74) of the gravitropic response is introduced in eqn (1.71)–(1.72) (without the advective term) to predict the gravitropic bending of an inclined stem, an unrealistic spatio-temporal dynamics is found. Instead of converging toward the vertical, the tip of the stem keeps oscillating back and forth, with regions of increasing curvature accumulating close to the base of the stem.⁸ This paradox was solved by adding to the gravitropic law (1.74) an additional term proportional to the local curvature, which counteracts the generation of curvature induced by gravity sensing:⁸

$$\Delta_{\text{prop}} = \left(\frac{\dot{\epsilon}_2 - \dot{\epsilon}_1}{\dot{\epsilon}_1 + \dot{\epsilon}_2} \right)_{\text{prop}} = -\gamma RC, \quad (1.74)$$

where γ is a dimensionless parameter. Such tendency of a stem or a shoot to perceive its own curvature and straighten was coined “autotropism” in early studies (see ref. 21 and 48 and older references therein) and latterly “proprioception”, by analogy with the sense of body perception in vertebrates.⁸ In plants, the mechanism of proprioception is still debated^{104,116} but its reality is well supported, in particular by experiments in microgravity environments which show that an initially curved stem spontaneously straightens during growth. Writing for simplicity $\sin \theta \approx \theta$ and neglecting the advection term in eqn (1.71) gives for the evolution of the curvature:

$$R \frac{\partial C}{\partial t} = \dot{\epsilon}(\beta \theta - \gamma RC). \quad (1.75)$$

^[4]This observation is valid as long as gravity intensity is high enough. In very low gravity environments (typically $g < 10^{-2} \text{ m s}^{-2}$), the avalanche time of the statoliths may become longer than the growth timescale $\dot{\epsilon}^{-1}$ so that statoliths have not the time to reach their equilibrium position before the plant bends. The gravitropic response then decreases and becomes null without gravity, as expected.

This mathematical model of gravitropism, which includes both graviperception and proprioception, was first introduced by Bastien *et al.*⁸ and coined the “AC model” (for Angle–Curvature). Unlike the purely gravitropic model, the AC model exhibits a steady solution ($\partial_t C = 0$) given by $\theta(s) = \theta_0 \exp(-s/L_c)$, where θ_0 is the inclination of the stem at the base and $L_c = \gamma R/\beta$ is a bending length scale. This steady shape is controlled by the balance number \mathcal{B} :

$$\mathcal{B} = \frac{L}{L_c} = \frac{L\beta}{\gamma R} \approx \mathcal{O}\left(\frac{\Delta_{\text{gravity}}}{\Delta_{\text{prop}}}\right), \quad (1.76)$$

which quantifies the ratio of the gravitropic term to the proprioceptive term. For $\mathcal{B} \gg 1$ ($L_c \ll L$), graviperception is large compare to proprioception and the plant rapidly recovers the vertical after a bending length L_c . In the opposite situation $\mathcal{B} \ll 1$ ($L_c \gg L$), proprioception overcomes graviperception and the plant does not recover the vertical over its length L . Note that the balance number \mathcal{B} not only controls the final shape of the plant but also its dynamics toward vertical: for large \mathcal{B} , the tip of the stem oscillates several times around the vertical before converging, which is not the case for small \mathcal{B} .⁸

The previous discussion shows that the perception of gravity alone through the sine law (1.74) does not enable a proper posture control in plants, and that an additional straightening or proprioceptive mechanism is needed. The AC model constitutes the building block from which additional effects may be considered. For instance, the gravitropic response exhibits several timescales not included in the simple sine law, such as a delay time before the beginning of bending and a memory time that filters rapid changes in inclination.²³ The purely kinematic model presented here can also be extended to add mechanical effects, such as elasticity and stem sagging under its own weight.²⁷ In this case, the actual (or observed) curvature C contains an elastic contribution due to the self-weight. It must thus be distinguished from the natural^{|||} curvature C^0 induced by differential growth and described by eqn (1.71). Finally, other kinds of tropisms and plant movements may be included in this framework, such as phototropism, thigmotropism or circumnutation – the spontaneous oscillation and circular movements of the tip of stems.^{1,10,106} Extension to three-dimensional growing rods, including torsion and helicity, are also available (see ref. 106 and references therein).

1.2.4.5 Growth in Thin Sheets and Morphogenesis

We have seen how differential growth across the thickness of a rod-shaped organ like a stem induces a change in natural curvature. When the organ

^{|||}The natural curvature is also called the intrinsic, or the spontaneous, curvature.

Box 1.5 Gravity sensing in plants: an active granular flow problem?

From tiny shoots to large trees, all plants are able to sense gravity and reorient their growth toward the vertical direction set by the gravitational field. This ability is important at early stages of development for roots to anchor in the soil and shoots to find light. It is also key throughout the plant's life, for the plant to maintain its upright position and not fall against its own weight. The detection of gravity in plants is known to originate in specialized cells (statocytes) containing dense starch grains (amyloplasts or statoliths); but how cells detect the statoliths and how this sensing is converted into a bending growth response at the organ level are still largely open questions (see, for example, the reviews^{101,103,105,109,158}).

Recent experiments studying the gravitropic response of shoots to hyper- and hypo-gravity conditions have shown that plants are not sensitive to the intensity of the gravity field, but only to the inclination against the direction of the gravity vector.^{24,124} The gravisensor in plants is thus a position sensor, not a force sensor. This finding is surprising because it implies that the pile of statoliths at the bottom of the cell move and respond to even the tiniest tilt. At first sight, such a behavior contradicts our knowledge of the physics of granular media, which stipulates that an assembly of grains cannot move below a critical avalanche angle set by friction and steric constraints between particles.³

The solution to this conundrum comes from the *in-situ* visualization of statolith movement in response to a large cell tilt¹³ (Figure 1.11b). Initially, statoliths flow in bulk like a granular “avalanche”, with a pile angle that rapidly relaxes toward a critical angle θ_c , as expected for a classical granular medium. However, over a long time the behavior strongly contrasts with that of a classical granular medium. Instead of being stuck at θ_c , the statolith pile keeps evolving and slowly creeps until its free surface recovers the horizontal, as a liquid would do. Investigation of statolith motion at the particle level reveals that this liquid-like behavior comes from the agitation of the statoliths, which helps the grains to unjam and flow even for very small inclinations. This agitation comes from cellular activity and not thermal agitation, as confirmed by comparison with the behavior of passive Brownian particles in the same geometry. It is likely to involve the dynamics of the actin-myosin network in the cytoskeleton, and its interaction with statoliths.

The remarkable sensitivity of plants to gravity therefore relies on an active granular material at the cellular level.¹³ This strategy, which combines local active noise and signal integration of statolith position, shares similarities with other biological sensors, such as hair cells¹⁰⁸ or tactile

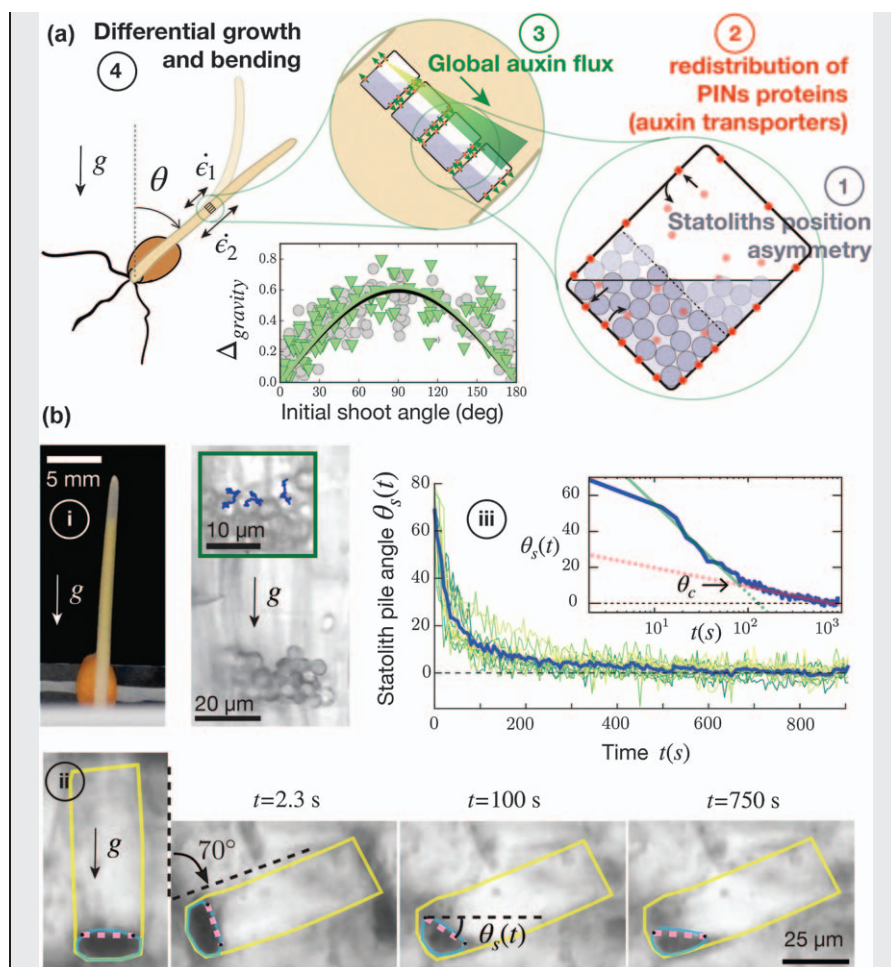


Figure 1.11 (a) Signaling pathway of plant gravitropism (adapted from ref. 90). The plot shows the gravitropic response of wheat coleoptiles to steady inclination²⁴ (sine law). (b) Flowing behavior of the plant gravisensors (statoliths). (i) Gravisensing cells of wheat coleoptile. (ii) In-situ visualization of statolith motion in response to a large tilt. The angle of the free-surface of the statolith pile (θ_s) first decreases rapidly toward a critical angle θ_c , then slowly creeps in order to recover the horizontal, as a liquid would do (iii, plot in lin-lin and log-lin scale). This pseudoliquid behavior comes from the agitation of statoliths by cell activity (blue trajectories in top-left image). Adapted from ref. 13, <https://doi.org/10.1073/pnas.1801895115>, under the terms of the CC BY 4.0 licence, <https://creativecommons.org/licenses/by/4.0/>.

whiskers.²⁸ Understanding the physics of such active particulate media is an exciting soft matter topic in itself, in addition to the biological motivations.

remains thin but extends in two directions, such as in a flat leaf, two different types of differential growth-induced shapes can occur***.

The first mode of deformation is similar to the one we just saw in the case of a one-dimensional stem and comes from a differential growth across the *thickness* of the sheet. In this situation, a natural curvature^{†††} C^0 in the direction of differential growth is generated, causing the sheet to curl into a cylindrical shape. Many plant leaves, for example grass blades or corn leaves, exhibit such rolled shapes induced by a differential expansion across the leaf thickness. However, when the leaf is curved in two perpendicular directions like a shell, bending in one direction is coupled to the other direction through the generation of in-plane tissue stresses, causing subtle rolling/unrolling mechanisms.¹⁰²

The second type of deformation is associated with differential *surface* growth: different regions of the sheet grow at different rates (Figure 1.10c). In general, these spatial variations in growth cannot happen without generating in-plane compressive stresses. For a thin sheet of lateral size L and thickness $h \ll L$, the energy cost of such compressive deformation is very high and the system prefers to bulge out of the plane. A non-zero natural Gauss curvature κ_G^0 is then created^{†††}. When the growth is larger in the center of the sheet than at the edges, the generated Gauss curvature is positive $\kappa_G^0 > 0$, *i.e.* the sheet deforms into a dome shape. In contrast, when the edges grow faster than the center, negative Gauss curvature $\kappa_G^0 < 0$ is created, resulting in rippling edges and saddle-like shapes. Many flat organs in plants and algae, such as leaves, blades or flowers, show this type of rippling at their edges, induced by faster growth at their periphery.^{29,83,142,143}

Overall, geometry and mechanics, in addition to genetics, play a primary role in morphogenesis and development – an idea promoted by pioneering scientists such as d'Arcy Thompson¹⁵⁶ and Paul Green.⁶¹ This role can be purely “passive”, as when differential growth generates out-of-plane bending to satisfy geometric compatibility. It can also be “active” and directly influence the molecular and genetic machinery of the plant, as we have seen in the case of the cell wall, where the stress in the wall controls the orientation of the cortical microtubules, which in turn affects wall anisotropy⁶³ (Figure 1.9b). Understanding such feedback between mechanical signals and biology is one of the main current challenges in plant morphogenesis.¹³⁹

***For general textbooks on the elasticity of plates and shells, see for example^{5,95,157} A mechanical description of thin growing sheets in the context of differential geometry can be found in ref. 44.

†††The natural (or intrinsic, or spontaneous) curvature is the curvature that remains when all external forces, geometrical frustrations or in-plane stresses are released. Experimentally, the natural curvature along a given direction in a plate or shell is found by cutting a thin strip in this direction and measuring the resulting curvature.

†††The Gauss curvature of a surface is defined by $\kappa_G = C_1 \times C_2$, where C_1 and C_2 are the two principal curvatures of the surface (*i.e.* the two extrema curvatures at the surface point considered). In practice, the natural Gauss curvature is found by cutting small discs onto the surface and measuring the two principal curvatures.

1.2.5 Mechanical Instabilities and Fast Movements

Throughout the chapter we have seen how plants, although lacking muscle, use gradients of water potential to transport water and perform various swelling or growth movements. The timescale of these water-driven movements is, however, constrained by a physical limit: for a cell or a tissue to swell, water must be transported from one place to another within the soft, porous plant material. We have seen that the shortest response time of this process is set by the cell relaxation time at the cellular level, and by the poroelastic time at the tissue level (Section 1.2.3). These timescales depend on the hydraulic and elastic properties of the medium and, more importantly, on the size of the system: the larger the organ, the greater the time required to produce purely hydraulic motion.

Plants have developed a simple and elegant strategy to overcome this hydraulic limit: the use of mechanical instabilities.^{50,52} The general principle is as follows: during a first “slow” phase, elastic deformation is stored in the cell wall due to a slow modification of the hydraulic or elastic properties (*e.g.* a water movement due to evaporation or active solute transport, a change of the mechanical properties of the wall, *etc.*). However, this elastic energy is not released because there exists an “energy barrier” in the system. When the stored elastic energy reaches a critical point, the energy barrier is crossed and a second “fast” phase occurs where the deformation in the wall is rapidly released and converted into a fast movement.

The existence of an energy barrier is the key ingredient for developing a mechanical instability. This barrier can be of molecular origin, as for bubble nucleation in a liquid under negative pressure or crack nucleation in a solid under tension. In this case, the cohesion between molecules is associated with an energy cost to create a new surface – the bubble or crack – in the medium. When the size of the bubble (or length of the crack) is large enough, the release of bulk energy is larger than the cost of surface energy; the bubble (or crack) then expands suddenly. Fracture propagation and its associated explosive elastic energy release is used by many plants to disperse their seeds or spores.^{37,46,74,76,133} The cavitation of bubbles in a liquid under tension, so harmful for trees, has been harnessed by some species of ferns to catapult their spores and thereby generate the fastest movement in the plant kingdom.^{81,113} The rich physics of cavitation in the context of plants is discussed in Chapter 4.

Mechanisms based on fracture propagation or bubble cavitation are one-shot, *irreversible* fast movements: once the stretched tissue is torn or the metastable liquid transformed into vapor, no resetting of motion is possible. A more flexible strategy to actuate *reversible* rapid movements consists of using an elastic or *snap-buckling instability*. A snap-buckling instability is the discontinuous transition between two states of minimal elastic energy in a slender body. In this case, the energy barrier comes from the existence of a geometrical constraint: the system cannot transit from one state to the other without passing through an intermediate shape that generates in-plane stresses. We have seen that for thin bodies these in-plane stresses are

associated with an important elastic energy cost. Elastic energy is then accumulated until it is so large that the barrier is crossed and the shape suddenly snaps through.

This principle is used by the carnivorous plant *Dionaea muscipula* (best known as the Venus flytrap) to trap insects^{53,123,136} (Figure 1.12a). The trap of the Venus flytrap consists of two doubly curved, shell-like lobes, which are convex (curved outward) in the initial state. Because bending such a shell requires crossing a stretching energy barrier (see below), the trap can store elastic energy without closing. However, when the inner hairs are triggered, the plant actively changes the natural curvature of its lobes in one direction. This is enough to cross the elastic energy barrier, leading to a sudden change of curvature and closure.

It is possible to quantify this mechanism using a minimal one-dimensional elastic energy model and scaling arguments.⁵³ Let consider a shell of typical size L , thickness h and Young's modulus E . From Hooke's law, the total elastic energy of the shell scales as: $\mathcal{E}_{el} \sim \frac{1}{2}EV\varepsilon^2$, where $V \sim hL^2$ is the volume of the shell and ε is the characteristic elastic strain associated to the deformation of the shell. When the shell is bent, two different modes of elastic deformation occur.⁸⁷ The first one is associated to pure bending, *i.e.* the fact that changing the curvature of a plate with respect to its natural curvature induces a gradient of elastic deformation within the thickness of the shell. The elastic strain associated to this bending mode is: $\varepsilon_{\text{bend}} \sim h(C - C^0)$, where C is the actual curvature and C^0 is the natural curvature. The corresponding bending elastic energy is thus:

$$\mathcal{E}_{\text{bend}} \sim Eh^3L^2(C - C^0)^2. \quad (1.77)$$

The second mode of deformation is related to geometrical incompatibility: it is not possible to bend and reverse the curvature of a shell without stretching or compressing its surface. This is a direct consequence of the Gauss' Theorema egregium,⁵ which implies that a surface cannot change its Gauss curvature without changing the natural length, or metric, of its surface. To estimate the stretching deformation $\varepsilon_{\text{stretch}}$ induced by such a change of Gauss curvature, let consider a shallow shell of radius of curvature $r \gg L$, which is deformed into a flat disc (Fig. 1.12b). Assuming that the length L along the diameter of the shell is conserved, the shell's perimeter must increase from πL_0 , where L_0 is the initial projected diameter, to πL , so that $\varepsilon_{\text{stretch}} \sim (L - L_0)/L_0$. Pythagoras's theorem implies that $\Delta^2 + (L_0^2/4) = L^2/4$ and $(r - \Delta)^2 + (L_0^2/4) = r^2$. Since $\Delta \ll r$ and $\Delta \ll L$, we have at first order: $\varepsilon_{\text{stretch}} \sim 2\Delta^2/L^2 \sim L^2/(32r^2) \propto L^2\kappa_G^0$, where $\kappa_G^0 = 1/r^2$ corresponds to the natural Gauss curvature of the shell. Here the Gauss curvature of the deformed state is zero since the disc is flat. This relationship can be generalized to a deformed state of arbitrary non-zero Gauss curvature as: $\varepsilon_{\text{stretch}} \sim L^2(\kappa - \kappa_G^0)$, where $\kappa_G = C^2$ is the Gauss curvature of the deformed state. Therefore, the elastic energy associated to the stretching mode is given by:

$$\mathcal{E}_{\text{stretch}} \sim EhL^6(\kappa_G - \kappa_G^0)^2 \sim EhL^6(C^2 - \kappa_G^0)^2. \quad (1.78)$$

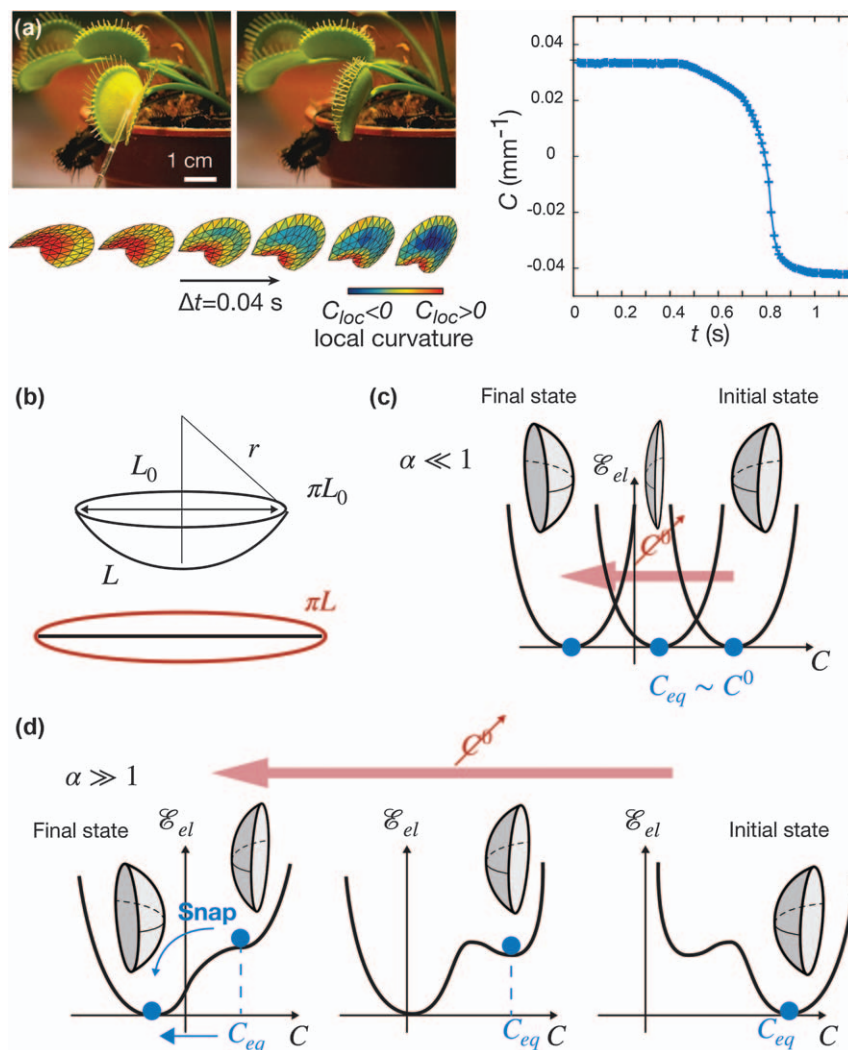


Figure 1.12 Rapid plant movements induced by a snap-buckling instability. (a) The carnivorous plant Venus flytrap (*Dionaea muscipula*) in the open (left image) and closed (right image) states. Bottom panel: three-dimensional shape reconstruction of the lobe during closure. Left panel: spatially averaged mean curvature of one lobe as function of time, showing a sudden transition from convex ($C > 0$) to concave ($C < 0$) (adapted from ref. 53). (b) Sketch of a shallow shell stretched into a flat disc, in which the shell's diameter L is conserved but the perimeter increases. (c) Elastic energy landscape for a thin shell when the bending energy dominates ($\alpha \ll 1$), showing a smooth transition from convex to concave as the natural curvature C^0 changes. C_{eq} is the equilibrium curvature that minimizes the energy. (d) When the stretching energy dominates ($\alpha > 1$), the energy landscape exhibits two local minima and the equilibrium shape suddenly snaps from convex to concave.

The total elastic energy of the shell is the sum of the bending energy (1.77) and stretching energy (1.78): $\mathcal{E}_{\text{el}} = \mathcal{E}_{\text{bend}} + \mathcal{E}_{\text{stretch}}$. It is convenient to make the curvatures dimensionless using the characteristic curvature $\sqrt{\kappa_G^0}$, such that: $\tilde{C} = C/\sqrt{\kappa_G^0}$, $\tilde{C}^0 = C^0/\sqrt{\kappa_G^0}$. Using eqn (1.77)–(1.78), the dimensionless total elastic energy of the shell $\tilde{\mathcal{E}}_{\text{el}} = \mathcal{E}_{\text{el}}/(EV(\kappa_G^0 h)^2)$ is then:

$$\tilde{\mathcal{E}}_{\text{el}} \sim (\tilde{C} - \tilde{C}^0)^2 + \alpha(\tilde{C}^2 - 1)^2,$$

with

$$\alpha \sim \frac{L^4 \kappa_G^0}{h^2} = \mathcal{O}\left(\frac{\mathcal{E}_{\text{stretching}}}{\mathcal{E}_{\text{bending}}}\right). \quad (1.80)$$

The parameter α quantifies the ratio of the stretching elastic energy to the bending elastic energy and depends only on the geometry of the shell: the thinner, wider or curved the shell, the greater the stretching energy compared to the bending energy. We see below that α determines how the shell flips from convex to concave when the natural curvature C^0 is gradually changed. To this end, we note that, for a given value of \tilde{C}^0 and α , the equilibrium shape of the shell \tilde{C}_{eq} is obtained by minimizing the total elastic energy with respect to \tilde{C} :

$$\left(\frac{\partial \tilde{\mathcal{E}}_{\text{el}}}{\partial \tilde{C}}\right)_{\tilde{C} = \tilde{C}_{\text{eq}}} = 0. \quad (1.81)$$

Figure 1.12c,d show qualitatively the shape of the total elastic energy as function of \tilde{C} when the natural curvature of the shell \tilde{C}^0 goes continuously from convex ($\tilde{C}^0 > 0$) to concave ($\tilde{C}^0 < 0$). For $\alpha \ll 1$, the bending energy dominates: the elastic energy exhibits only one minimum and the curvature of the shell at equilibrium is always very close to the natural curvature $C_{\text{eq}} \approx C^0$. Therefore, when the natural curvature changes from positive to negative, the shell shape follows the natural curvature and smoothly changes from convex to concave (Figure 1.12c). The situation is markedly different for $\alpha \gtrsim 1$ (Figure 1.12d). In this case, the stretching energy is large and the total elastic energy (1.79) may exhibit two local minima separated by an energy barrier, depending on the value of the natural curvature. As shown in Fig. 1.12d, when the sign of the natural curvature changes, the system initially remains stuck in the first local minimum of convex shape, until the energy barrier disappears and the shell suddenly flips to the second minimum of energy, corresponding to the concave shape. Therefore, a small change of natural curvature (the internal motor of the motion) may lead to a very large change of actual curvature from convex to concave. This is the amplification mechanism used by the Venus flytrap and other carnivorous plants to speed up their motion and engulf their preys.^{53,162}

The active process by which plants like the Venus flytrap trigger the instability and overcome the energy barrier is still not fully elucidated, raising

interesting questions about signaling and fast mechanical actuation at the molecular level.^{50,66,154} However, the general principle of using an elastic instability to overcome the hydraulic limit and amplify the speed of motion is robust and weakly depends on these microscopic details.¹⁴⁶ This strategy has already inspired several artificial devices, such as fast soft actuators and jumping robots.^{73,79,94,168} More generally, the non-muscular movements of plants offer a wealth of mechanisms worth studying from a physics and engineering perspective.^{19,22,140} Biomimetic applications of plant movements are further discussed in Chapter 8.

Acknowledgements

I would like to thank the whole scientific community of Plant Biomech' and GDR PhyP ("Plant Biophysics and biomechanics", CNRS no 2007), from whom I learned most of the ideas and concepts discussed in this chapter. I particularly thank Jacques Dumais and Bruno Moulia who introduced me to the fascinating field of plant biomechanics almost 20 years ago. This work was supported by the European Research Council (ERC) under the European Union's Horizon 2020 research and innovation program (Grant 647384).

References

1. D. Agostinelli, A. Lucantonio, G. Noselli and A. DeSimone, Nutations in growing plant shoots: The role of elastic deformations due to gravity loading, *J. Mech. Phys. Solids*, 2020, **136**, 103702.
2. O. Ali and J. Traas, Force-driven polymerization and turgor-induced wall expansion, *Trends Plant Sci.*, 2016, **21**(5), 398–409.
3. B. Andreotti, Y. Forterre and O. Pouliquen, *Granular Media: Between Fluid and Solid*, Cambridge University Press, 2013.
4. S. Armon, E. Efrati, R. Kupferman and E. Sharon, Geometry and mechanics in the opening of chiral seed pods, *Science*, 2011, **333**(6050), 1726–1730.
5. B. Audoly and Y. Pomeau, *Elasticity and Geometry: From Hair Curls to the Non-linear Response of Shells*, Oxford university press, 2010.
6. N. J. Balmforth, I. A. Frigaard and G. Ovarlez, Yielding to stress: recent developments in viscoplastic fluid mechanics, *Annu. Rev. Fluid Mech.*, 2014, **46**, 121–146.
7. A. Barbacci, M. Lahaye and V. Magnenet, Another brick in the cell wall: biosynthesis dependent growth model, *PLoS One*, 2013, **8**(9), e74400.
8. R. Bastien, T. Bohr, B. Moulia and S. Douady, Unifying model of shoot gravitropism reveals proprioception as a central feature of posture control in plants, *Proc. Natl. Acad. Sci.*, 2013, **110**(2), 755–760.
9. R. Bastien, S. Douady and B. Moulia, A unifying modeling of plant shoot gravitropism with an explicit account of the effects of growth, *Front. Plant Sci.*, 2014, **5**, 136.

10. R. Bastien, S. Douady and B. Moulia, A unified model of shoot tropism in plants: photo-, gravi-and proprioception, *PLoS Comput. Biol.*, 2015, **11**(2), e1004037.
11. L. Beauzamy, J. Derr and A. Boudaoud, Quantifying hydrostatic pressure in plant cells by using indentation with an atomic force microscope, *Biophys. J.*, 2015, **108**(10), 2448–2456.
12. T. Bertrand, J. Peixinho, S. Mukhopadhyay and C. W. MacMinn, Dynamics of swelling and drying in a spherical gel, *Phys. Rev. Appl.*, 2016, **6**(6), 064010.
13. A. Bérut, H. Chauvet, V. Legué, B. Moulia, O. Pouliquen and Y. Forterre, Gravisensors in plant cells behave like an active granular liquid, *Proc. Natl. Acad. Sci.*, 2018, **115**(20), 5123–5128.
14. A. Boudaoud, An introduction to the mechanics of morphogenesis for plant biologists, *Trends Plant Sci.*, 2010, **15**(6), 353–360.
15. F. Boudon, J. Chopard, O. Ali, B. Gilles, O. Hamant, A. Boudaoud, J. Traas and C. Godin, A computational framework for 3d mechanical modeling of plant morphogenesis with cellular resolution, *PLoS Comput. Biol.*, 2015, **11**(1), e1003950.
16. J. S. Boyer, A. Cavalieri and E.-D. Schulze, Control of the rate of cell enlargement: excision, wall relaxation, and growth-induced water potentials, *Planta*, 1985, **163**(4), 527–543.
17. J. S. Boyer and W. K. Silk, Hydraulics of plant growth, *Funct. Plant Biol.*, 2004, **31**(8), 761–773.
18. B. Bozorg, P. Krupinski and H. Jönsson, A continuous growth model for plant tissue, *Phys. Biol.*, 2016, **13**(6), 065002.
19. I. Burgert and P. Fratzl, Actuation systems in plants as prototypes for bioinspired devices, *Philos. Trans. R. Soc., A*, 2009, **367**(1893), 1541–1557.
20. N. Carpita, D. Sabulase, D. Montezinos and D. P. Delmer, Determination of the pore size of cell walls of living plant cells, *Science*, 1979, **205**(4411), 1144–1147.
21. D. K. Chapman, A. Johnsson, C. Karlsson, A. Brown and D. Heathcote, Gravitropically-stimulated seedlings show autotropism in weightlessness, *Physiol. Plant.*, 1994, **90**(1), 157–162.
22. V. Charpentier, P. Hannequart, S. Adriaenssens, O. Baverel, E. Viglino and S. Eisenman, Kinematic amplification strategies in plants and engineering, *Smart Mater. Struct.*, 2017, **26**(6), 063002.
23. H. Chauvet, B. Moulia, V. Legué, Y. Forterre and O. Pouliquen, Revealing the hierarchy of processes and time-scales that control the tropic response of shoots to gravi-stimulations, *J. Exp. Bot.*, 2019, **70**(6), 1955–1967.
24. H. Chauvet, O. Pouliquen, Y. Forterre, V. Legué and B. Moulia, Inclination not force is sensed by plants during shoot gravitropism, *Sci. Rep.*, 2016, **6**(1), 1–8.
25. Y. Chebli and A. Geitmann, Cellular growth in plants requires regulation of cell wall biochemistry, *Curr. Opin. Cell Biol.*, 2017, **44**, 28–35.

26. I. Cheddadi, M. Génard, N. Bertin and C. Godin, Coupling water fluxes with cell wall mechanics in a multicellular model of plant development, *PLoS Comput. Biol.*, 2019, **15**(6), e1007121.
27. R. Chelakkot and L. Mahadevan, On the growth and form of shoots, *J. R. Soc., Interface*, 2017, **14**(128), 20170001.
28. L. N. Claverie, Y. Boubenec, G. Debrégeas, A. M. Prevost and E. Wandersman, Whisker contact detection of rodents based on slow and fast mechanical inputs, *Front. Behav. Neurosci.*, 2017, **10**, 251.
29. E. Coen, A.-G. Rolland-Lagan, M. Matthews, J. A. Bangham and P. Prusinkiewicz, The genetics of geometry, *Proc. Natl. Acad. Sci.*, 2004, **101**(14), 4728–4735.
30. D. Cosgrove and E. Steudle, Water relations of growing pea epicotyl segments, *Planta*, 1981, **153**(4), 343–350.
31. D. J. Cosgrove, Cell wall yield properties of growing tissue: evaluation by in vivo stress relaxation, *Plant Physiol.*, 1985, **78**(2), 347–356.
32. D. J. Cosgrove, Growth of the plant cell wall, *Nat. Rev. Mol. Cell Biol.*, 2005, **6**(11), 850–861.
33. D. J. Cosgrove, Nanoscale structure, mechanics and growth of epidermal cell walls, *Curr. Opin. Plant Biol.*, 2018, **46**, 77–86.
34. O. Coussy, *Poromechanics*, John Wiley & Sons, 2004.
35. J. Dainty, Water relations of plant cells, *Advances in Botanical Research*, Elsevier, 1963, vol. 1, pp. 279–326.
36. C. Dawson, J. F. Vincent and A.-M. Rocca, How pine cones open, *Nature*, 1997, **390**(6661), 668.
37. R. D. Deegan, Finessing the fracture energy barrier in ballistic seed dispersal, *Proc. Natl. Acad. Sci.*, 2012, **109**(14), 5166–5169.
38. H. H. Dixon and J. Joly, *Xii. on the ascent of sap. Philos. Trans. R. Soc., B*, 1895, **186**, 563–576.
39. J. Dumais and Y. Forterre, “vegetable dynamicks”: the role of water in plant movements, *Annu. Rev. Fluid Mech.*, 2012, **44**, 453–478.
40. J. Dumais, S. L. Shaw, C. R. Steele, S. R. Long and P. M. Ray, An anisotropic-viscoplastic model of plant cell morphogenesis by tip growth, *Int. J. Dev. Biol.*, 2006, **50**, 209–222.
41. P. Durand-Smet, E. Gauquelin, N. Chastrette, A. Boudaoud and A. Asnacios, Estimation of turgor pressure through comparison between single plant cell and pressurized shell mechanics, *Phys. Biol.*, 2017, **14**(5), 055002.
42. R. Dyson, L. Band and O. Jensen, A model of crosslink kinetics in the expanding plant cell wall: yield stress and enzyme action, *J. Theor. Biol.*, 2012, **307**, 125–136.
43. R. Dyson and O. Jensen, A fibre-reinforced fluid model of anisotropic plant cell growth, *J. Fluid Mech.*, 2010, **655**, 472.
44. E. Efrati, E. Sharon and R. Kupferman, The metric description of elasticity in residually stressed soft materials, *Soft Matter*, 2013, **9**(34), 8187–8197.

45. R. Elbaum, L. Zaltzman, I. Burgert and P. Fratzl, The role of wheat awns in the seed dispersal unit, *Science*, 2007, **316**(5826), 884–886.
46. D. Evangelista, S. Hotton and J. Dumais, The mechanics of explosive dispersal and self-burial in the seeds of the filaree, *erodium cicutarium* (geraniaceae), *J. Exp. Biol.*, 2011, **214**(4), 521–529.
47. A. Finkelstein, *Water Movement Through Lipid Bilayers, Pores, and Plasma Membranes: Theory and Reality*, John Wiley and Sons, 1987.
48. R. Firn and J. Digby, A study of the autotropic straightening reaction of a shoot previously curved during geotropism, *Plant, Cell Environ.*, 1979, **2**(2), 149–154.
49. A. Fleischer, M. A. O'Neill and R. Ehwald, The pore size of non-graminaceous plant cell walls is rapidly decreased by borate ester cross-linking of the pectic polysaccharide rhamnogalacturonan ii, *Plant Physiol.*, 1999, **121**(3), 829–838.
50. Y. Forterre, Slow, fast and furious: understanding the physics of plant movements, *J. Exp. Bot.*, 2013, **64**(15), 4745–4760.
51. Y. Forterre and J. Dumais, Generating helices in nature, *Science*, 2011, **333**(6050), 1715–1716.
52. Y. Forterre, P. Marmottant, C. Quilliet and X. Noblin, Physics of rapid movements in plants, *Europhys. News*, 2016, **47**(1), 27–30.
53. Y. Forterre, J. M. Skotheim, J. Dumais and L. Mahadevan, How the venus flytrap snaps, *Nature*, 2005, **433**(7024), 421–425.
54. A. Fowler, Glaciers and ice sheets, *The Mathematics of Models for Climatology and Environment*, Springer, 1997, pp. 301–336.
55. P. J. Franks, T. N. Buckley, J. C. Shope and K. A. Mott, Guard cell volume and pressure measured concurrently by confocal microscopy and the cell pressure probe, *Plant Physiol.*, 2001, **125**(4), 1577–1584.
56. A. Geitmann, Experimental approaches used to quantify physical parameters at cellular and subcellular levels, *Am. J. Bot.*, 2006, **93**(10), 1380–1390.
57. L. Gibson and M. Ashby, *Cellular Solids: Structure and Properties*, cambridge univ press, Cambridge, UK, 1999.
58. S. Gilroy and P. Masson. *Plant Tropisms*, Blackwell Publishing, Oxford, UK, 2008.
59. S. Gravelle, L. Joly, F. Detcheverry, C. Ybert, C. Cottin-Bizonne and L. Bocquet. Optimizing water permeability through the hourglass shape of aquaporins. *Proc. Natl. Acad. Sci.*, 2013, **110**(41):16367–16372.
60. P. Green, R. Erickson and J. Buggy, Metabolic and physical control of cell elongation rate: in vivo studies in nitella, *Plant Physiol.*, 1971, **47**(3), 423–430.
61. P. B. Green, Organogenesis-a biophysical view, *Annu. Rev. Plant Physiol.*, 1980, **31**(1), 51–82.
62. P. B. Green and F. W. Stanton, Turgor pressure: direct manometric measurement in single cells of nitella, *Science*, 1967, **155**(3770), 1675–1676.

63. O. Hamant, M. G. Heisler, H. Jönsson, P. Krupinski, M. Uyttewaal, P. Bokov, F. Corson, P. Sahlin, A. Boudaoud and E. M. Meyerowitz, *et al.*, Developmental patterning by mechanical signals in arabidopsis, *Science*, 2008, **322**(5908), 1650–1655.
64. O. Hamant, D. Inoue, D. Bouchez, J. Dumais and E. Mjolsness, Are microtubules tension sensors?, *Nat. Commun.*, 2019, **10**(1), 1–12.
65. E. S. Haswell, R. Peyronnet, H. Barbier-Brygoo, E. M. Meyerowitz and J.-M. Frachisse, Two mscs homologs provide mechanosensitive channel activities in the arabidopsis root, *Curr. Biol.*, 2008, **18**(10), 730–734.
66. R. Hedrich and E. Neher, Venus flytrap: how an excitable, carnivorous plant works, *Trends Plant Sci.*, 2018, **23**(3), 220–234.
67. Z. Hejnowicz and A. Sievers, Tissue stresses in organs of herbaceous plants: I. poisson ratios of tissues and their role in determination of stresses, *J. Exp. Bot.*, 1995, **46**, 1035–1043.
68. V. Hernández-Hernández, M. Bentez and A. Boudaoud, Interplay between turgor pressure and plasmodesmata during plant development, *J. Exp. Bot.*, 2020, **71**(3), 768–777.
69. N. Hervieux, M. Dumond, A. Sapala, A.-L. Routier-Kierzkowska, D. Kierzkowski, A. H. Roeder, R. S. Smith, A. Boudaoud and O. Hamant, A mechanical feedback restricts sepal growth and shape in arabidopsis, *Curr. Biol.*, 2016, **26**(8), 1019–1028.
70. A. N. Heyn, Further investigations on the mechanism of cell elongation and the properties of the cell wall in connection with elongation, *Protoplasma*, 1933, **19**(1), 78–96.
71. B. S. Hill and G. P. Findlay, The power of movement in plants: the role of osmotic machines, *Q. Rev. Biophys.*, 1981, **14**(2), 173–222.
72. H. Höfte, A. Peaucelle and S. Braybrook, Cell wall mechanics and growth control in plants: the role of pectins revisited, *Front. Plant Sci.*, 2012, **3**, 121.
73. D. P. Holmes and A. J. Crosby, Snapping surfaces, *Adv. Mater.*, 2007, **19**(21), 3589–3593.
74. C. T. Ingold, *et al.*, Spore liberation, *Spore liberation*, 1965.
75. K. H. Jensen, K. Berg-Sørensen, H. Bruus, N. M. Holbrook, J. Liesche, A. Schulz, M. A. Zwieniecki and T. Bohr, Sap flow and sugar transport in plants, *Rev. Mod. Phys.*, 2016, **88**(3), 035007.
76. L. Jost and R. J. Harvey-Gibson, *Lectures on Plant Physiology*, Clarendon Press, 1907.
77. O. Kedem and A. Katchalsky, Thermodynamic analysis of the permeability of biological membranes to non-electrolytes, *Biochem. Biophys. Acta*, 1958, **27**, 229–246.
78. D. Kierzkowski, N. Nakayama, A.-L. Routier-Kierzkowska, A. Weber, E. Bayer, M. Schorderet, D. Reinhardt, C. Kuhlemeier and R. S. Smith, Elastic domains regulate growth and organogenesis in the plant shoot apical meristem, *Science*, 2012, **335**(6072), 1096–1099.
79. S.-W. Kim, J.-S. Koh, J.-G. Lee, J. Ryu, M. Cho and K.-J. Cho, Flytrap-inspired robot using structurally integrated actuation based on

- bistability and a developable surface, *Bioinspiration Biomimetics*, 2014, **9**(3), 036004.
80. Y. X. Kim and E. Steudle, Light and turgor affect the water permeability (aquaporins) of parenchyma cells in the midrib of leaves of zea mays, *J. Exp. Bot.*, 2007, **58**(15–16), 4119–4129.
 81. A. L. King, The spore discharge mechanism of common ferns, *Proc. Natl. Acad. Sci. U. S. A.*, 1944, **30**(7), 155.
 82. J. Knoblauch, D. L. Mullendore, K. H. Jensen and M. Knoblauch, Pico gauges for minimally invasive intracellular hydrostatic pressure measurements, *Plant Physiol.*, 2014, **166**(3), 1271–1279.
 83. M. A. Koehl and W. K. Silk, How kelp in drag lose their ruffles: environmental cues, growth kinematics, and mechanical constraints govern curvature, *J. Exp. Bot.*, 2021, **72**(10), 3677–3687.
 84. E. M. Kramer and D. R. Myers, Osmosis is not driven by water dilution, *Trends Plant Sci.*, 2013, **18**(4), 195–197.
 85. P. J. Kramer and J. S. Boyer, *Water Relations of Plants and Soils*, Academic press, 1995.
 86. U. Kutschera, Regulation of cell expansion, *The Cytoskeletal Basis of Plant Growth and Form*, 1991, pp. 85–99.
 87. L. D. Landau and E. M. Lifshitz, *et al.*, *Theory of Elasticity*, Pergamon Press, Oxford New York, 1986, vol. 7.
 88. T. Lawson and J. Matthews, Guard cell metabolism and stomatal function, *Annu. Rev. Plant Biol.*, 2020, **71**, 273–302.
 89. P. Lehmann and D. Or, Effects of stomata clustering on leaf gas exchange, *New Phytol.*, 2015, **207**(4), 1015–1025.
 90. N. Levernier, O. Pouliquen and Y. Forterre, An integrative model of plant gravitropism linking statoliths position and auxin transport, *Front. Plant Sci.*, 2021, **12**, 474.
 91. P. M. Lintilhac, C. Wei, J. J. Tanguay and J. O. Outwater, Ball tonometry: a rapid, nondestructive method for measuring cell turgor pressure in thin-walled plant cells, *J. Plant Growth Regul.*, 2000, **19**(1), 90–97.
 92. J. A. Lockhart, An analysis of irreversible plant cell elongation, *J. Theor. Biol.*, 1965, **8**(2), 264–275.
 93. Y. Long, I. Cheddadi, G. Mosca, V. Mirabet, M. Dumond, A. Kiss, J. Traas, C. Godin and A. Boudaoud, Cellular heterogeneity in pressure and growth emerges from tissue topology and geometry, *Curr. Biol.*, 2020, **30**(8), 1504–1516.
 94. D. Lunni, M. Cianchetti, C. Filippeschi, E. Sinibaldi and B. Mazzolai, Plant-inspired soft bistable structures based on hygroscopic electrospun nanofibers, *Adv. Mater. Interfaces*, 2020, **7**(4), 1901310.
 95. E. H. Mansfield, *The Bending and Stretching of Plates*, Cambridge university press, 1989.
 96. C. Maurel, L. Verdoucq, D.-T. Luu and V. Santoni, Plant aquaporins: membrane channels with multiple integrated functions, *Annu. Rev. Plant Biol.*, 2008, **59**, 595–624.

97. P. Milani, S. A. Braybrook and A. Boudaoud, Shrinking the hammer: micromechanical approaches to morphogenesis, *J. Exp. Bot.*, 2013, **64**(15), 4651–4662.
98. P. Milani, M. Gholamirad, J. Traas, A. Arnéodo, A. Boudaoud, F. Argoul and O. Hamant, In vivo analysis of local wall stiffness at the shoot apical meristem in arabidopsis using atomic force microscopy, *Plant J.*, 2011, **67**(6), 1116–1123.
99. F. J. Molz and J. S. Boyer, Growth-induced water potentials in plant cells and tissues, *Plant Physiol.*, 1978, **62**(3), 423–429.
100. F. J. Molz and E. Ikenberry, Water transport through plant cells and cell walls: theoretical development, *Soil Sci. Soc. Am. J.*, 1974, **38**(5), 699–704.
101. M. T. Morita, Directional gravity sensing in gravitropism, *Annu. Rev. Plant Biol.*, 2010, **61**, 705–720.
102. B. Moulia, Leaves as shell structures: double curvature, auto-stresses, and minimal mechanical energy constraints on leaf rolling in grasses, *J. Plant Growth Regul.*, 2000, **19**(1), 19–30.
103. B. Moulia, R. Bastien, H. Chauvet-Thiry and N. Leblanc-Fournier, Posture control in land plants: growth, position sensing, proprioception, balance, and elasticity, *J. Exp. Bot.*, 2019, **70**(14), 3467–3494.
104. B. Moulia, S. Douady and O. Hamant, Fluctuations shape plants through proprioception, *Science*, 2021, **372**(6540), eabc6868.
105. B. Moulia and M. Fournier, The power and control of gravitropic movements in plants: a biomechanical and systems biology view, *J. Exp. Bot.*, 2009, **60**(2), 461–486.
106. D. E. Moulton, H. Oliveri and A. Goriely, Multiscale integration of environmental stimuli in plant tropism produces complex behaviors, *Proc. Natl. Acad. Sci.*, 2020, **117**(51), 32226–32237.
107. E. Münch, Die stoffbewegung in der pflanze, fischer, jena, 1930.
108. B. Nadrowski, P. Martin and F. Jülicher, Active hair-bundle motility harnesses noise to operate near an optimum of mechanosensitivity, *Proc. Natl. Acad. Sci.*, 2004, **101**(33), 12195–12200.
109. M. Nakamura, T. Nishimura and M. T. Morita, Gravity sensing and signal conversion in plant gravitropism, *J. Exp. Bot.*, 2019, **70**(14), 3495–3506.
110. K. J. Niklas and H.-C. Spatz, *Plant Physics*, University of Chicago Press, 2012.
111. S. B. Nilsson, C. H. Hertz and S. Falk, On the relation between turgor pressure and tissue rigidity. ii: Theoretical calculations on model systems, *Physiol. Plant.*, 1958, **11**(4), 818–837.
112. P. S. Nobel *et al.*, *Physicochemical & Environmental Plant Physiology*, Academic press, 1999.
113. X. Noblin, N. Rojas, J. Westbrook, C. Llorens, M. Argentina and J. Dumais, The fern sporangium: a unique catapult, *Science*, 2012, **335**(6074), 1322.
114. B. Nordbring-Hertz, H.-B. Jansson, Y. Persson, E. Friman and C. Dackman, Nematophagous fungi, In TIB AV-PORTAL, <https://av.tib.eu/media/14259>.

115. B. Nordbring-Hertz, H.-B. Jansson and A. Tunlid, Nematophagous fungi, *Encyclopedia of Life Sciences*, Wiley Online Library, 2006, pp. 173–204.
116. K. Okamoto, H. Ueda, T. Shimada, K. Tamura, T. Kato, M. Tasaka, M. T. Morita and I. Hara-Nishimura, Regulation of organ straightening and plant posture by an actin–myosin xi cytoskeleton, *Nat. Plants*, 2015, **1**(4), 1–7.
117. H. Oliveri, On the role of mechanical feedback in plant morphogenesis, PhD thesis, Université Montpellier, 2019.
118. H. Oliveri, J. Traas, C. Godin and O. Ali, Regulation of plant cell wall stiffness by mechanical stress: a mesoscale physical model, *J. Math. Biol.*, 2019, **78**(3), 625–653.
119. J. K. Ortega, Augmented growth equation for cell wall expansion, *Plant Physiol.*, 1985, **79**(1), 318–320.
120. T. Pedley, Calculation of unstirred layer thickness in membrane transport experiments: a survey, *Q. Rev. Biophys.*, 1983, **16**(2), 115–150.
121. B. Péret, G. Li, J. Zhao, L. R. Band, U. Voß, O. Postaire, D.-T. Luu, O. Da Ines, I. Casimiro, M. Lucas, D. M. Wells, L. Lazzerini, P. Nacry, J. R. King, O. E. Jensen, A. R. SchÅøner, C. Maurel and M. J. Bennett, Auxin regulates aquaporin function to facilitate lateral root emergence, *Nat. Cell Biol.*, 2012, **14**(10), 991–998.
122. J. Philip, Propagation of turgor and other properties through cell aggregations, *Plant Physiol.*, 1958, **33**(4), 271.
123. S. Poppinga and M. Joyeux, Different mechanics of snap-trapping in the two closely related carnivorous plants *dionaea muscipula* and *aldrovanda vesiculosa*, *Phys. Rev. E*, 2011, **84**(4), 041928.
124. O. Pouliquen, Y. Forterre, A. Bérut, H. Chauvet, F. Bizet, V. Legue and B. Moulia, A new scenario for gravity detection in plants: the position sensor hypothesis, *Phys. Biol.*, 2017, **14**(3), 035005.
125. M. Probine and R. Preston, Cell growth and the structure and mechanical properties of the wall in internodal cells of *nitella opaca*: II. mechanical properties of the walls, *J. Exp. Bot.*, 1962, **13**(1), 111–127.
126. T. E. Proseus, J. K. Ortega and J. S. Boyer, Separating growth from elastic deformation during cell enlargement, *Plant Physiol.*, 1999, **119**(2), 775–784.
127. T. E. Proseus, G.-L. Zhu and J. S. Boyer, Turgor, temperature and the growth of plant cells: using *chara corallina* as a model system, *J. Exp. Bot.*, 2000, **51**(350), 1481–1494.
128. P. S. Raux, S. Gravelle and J. Dumais, Design of a unidirectional water valve in *tillandsia*, *Nat. Commun.*, 2020, **11**(1), 1–7.
129. M. Rivière, Y. Corre, A. Peaucelle, J. Derr and S. Douady, The hook shape of growing leaves results from an active regulatory process, *J. Exp. Bot.*, 2020, **71**(20), 6408–6417.
130. F. E. Rockwell, N. M. Holbrook and A. D. Stroock, Leaf hydraulics i: Scaling transport properties from single cells to tissues, *J. Theor. Biol.*, 2014, **340**, 251–266.

131. F. E. Rockwell, N. M. Holbrook and A. D. Stroock, Leaf hydraulics ii: vascularized tissues, *J. Theor. Biol.*, 2014, **340**, 267–284.
132. E. R. Rojas, S. Hotton and J. Dumais, Chemically mediated mechanical expansion of the pollen tube cell wall, *Biophys. J.*, 2011, **101**(8), 1844–1853.
133. A. Rolena, M. Paetkau, K. A. Ross, D. V. Godfrey, J. S. Church and C. R. Friedman, Thermogenesis-triggered seed dispersal in dwarf mistletoe, *Nat. Commun.*, 2015, **6**(1), 1–5.
134. J.-P. Rospars and N. Meyer-Vernet, Force per cross-sectional area from molecules to muscles: a general property of biological motors, *R. Soc., Open Sci.*, 2016, **3**(7), 160313.
135. A.-L. Routier-Kierzkowska, A. Weber, P. Kochova, D. Felekis, B. J. Nelson, C. Kuhlmeier and R. S. Smith, Cellular force microscopy for in vivo measurements of plant tissue mechanics, *Plant Physiol.*, 2012, **158**(4), 1514–1522.
136. R. Sachse, A. Westermeier, M. Mylo, J. Nadasdi, M. Bischoff, T. Speck and S. Poppinga, Snapping mechanics of the venus flytrap (*dionaea muscipula*), *Proc. Natl. Acad. Sci.*, 2020, **117**(27), 16035–16042.
137. L. Sack and N. M. Holbrook, Leaf hydraulics, *Annu. Rev. Plant Biol.*, 2006, **57**, 361–381.
138. A. Sampathkumar, P. Krupinski, R. Wightman, P. Milani, A. Berquand, A. Boudaoud, O. Hamant, H. Jönsson and E. M. Meyerowitz, Sub-cellular and supracellular mechanical stress prescribes cytoskeleton behavior in arabidopsis cotyledon pavement cells, *eLife*, 2014, **3**, e01967.
139. A. Sampathkumar, A. Yan, P. Krupinski and E. M. Meyerowitz, Physical forces regulate plant development and morphogenesis, *Curr. Biol.*, 2014, **24**(10), R475–R483.
140. S. Schleicher, J. Lienhard, S. Poppinga, T. Speck and J. Knippers, A methodology for transferring principles of plant movements to elastic systems in architecture, *Comput. -Aided Des.*, 2015, **60**, 105–117.
141. J. Schroeder, R. Hedrich and J. Fernandez, Potassium-selective single channels in guard cell protoplasts of *vicia faba*, *Nature*, 1984, **312**(5992), 361–362.
142. J. M. Selker, G. L. Steucek and P. B. Green, Biophysical mechanisms for morphogenetic progressions at the shoot apex, *Dev. Biol.*, 1992, **153**(1), 29–43.
143. E. Sharon, B. Roman, M. Marder, G.-S. Shin and H. L. Swinney, Buckling cascades in free sheets, *Nature*, 2002, **419**(6907), 579.
144. W. K. Silk, Quantitative descriptions of development, *Annu. Rev. Plant Physiol.*, 1984, **35**(1), 479–518.
145. W. K. Silk and R. O. Erickson, Kinematics of hypocotyl curvature, *Am. J. Bot.*, 1978, **65**(3), 310–319.
146. J. M. Skotheim and L. Mahadevan, Physical limits and design principles for plant and fungal movements, *Science*, 2005, **308**(5726), 1308–1310.

147. E. Steudle, Water flow in plants and its coupling to other processes: An overview, *Methods Enzymol.*, 1989, **174**, 183–225.
148. E. Steudle, The biophysics of plant water: compartmentation, coupling with metabolic processes, and flow of water in plant roots, *Water and life*, Springer, 1992, pp. 173–204.
149. E. Steudle. Pressure probe technique: basic principles and application to studies of water and solute relations at the cell, tissue and organ level, *Water deficits. Plant responses from cell to community*, 1993, pp. 5–36.
150. E. Steudle and U. Zimmermann, Determination of the hydraulic conductivity and of reflection coefficients in nitella flexilis by means of direct cell-turgor pressure measurements, *Biochim. Biophys. Acta, Biomembr.*, 1974, **332**(3), 399–412.
151. E. Steudle, U. Zimmermann and U. Lüttge, Effect of turgor pressure and cell size on the wall elasticity of plant cells, *Plant Physiol.*, 1977, **59**(2), 285–289.
152. H. Stoeckel and K. Takeda, Calcium-sensitivity of the plasmalemmal delayed rectifier potassium current suggests that calcium influx in pulvinar protoplasts from mimosa pudica L. can be revealed by hyperpolarization, *J. Membr. Biol.*, 1995, **146**(2), 201–209.
153. A. D. Stroock, V. V. Pagay, M. A. Zwieniecki and N. Michele Holbrook, The physicochemical hydrodynamics of vascular plants, *Annu. Rev. Fluid Mech.*, 2014, **46**, 615–642.
154. H. Suda, H. Mano, M. Toyota, K. Fukushima, T. Mimura, I. Tsutsui, R. Hedrich, Y. Tamada and M. Hasebe, Calcium dynamics during trap closure visualized in transgenic venus flytrap, *Nat. Plants*, 2020, **6**(10), 1219–1224.
155. L. Taiz and E. Zeiger, *Plant Physiology*, Sinauer Associates, Inc. Publishers, Sunderland, MA, 2002, 3:484.
156. D. W. Thompson *et al.*, On growth and form, *On Growth and Form*, 1942.
157. S. P. Timoshenko and S. Woinowsky-Krieger, *Theory of Plates and Shells*, McGraw-Hill, 1959.
158. M. Toyota and S. Gilroy, Gravitropism and mechanical signaling in plants, *Am. J. Bot.*, 2013, **100**(1), 111–125.
159. D.-C. Trinh, J. Alonso-Serra, M. Asaoka, L. Colin, M. Cortes, A. Malivert, S. Takatani, F. Zhao, J. Traas, C. Trehin and O. Hamant, How mechanical forces shape plant organs, *Curr. Biol.*, 2021, **31**(3), R143–R159.
160. M. T. Tyree and M. H. Zimmermann, *Xylem Structure and the Ascent of Sap*, Springer, 2002.
161. D. Vella, A. Ajdari, A. Vaziri and A. Boudaoud, Indentation of ellipsoidal and cylindrical elastic shells, *Phys. Rev. Lett.*, 2012, **109**(14), 144302.
162. O. Vincent, C. Weißkopf, S. Poppinga, T. Masselter, T. Speck, M. Joyeux, C. Quilliet and P. Marmottant, Ultra-fast underwater suction traps, *Proc. R. Soc. B*, 2011, **278**(1720), 2909–2914.

163. M. Warner, B. Thiel and A. Donald, The elasticity and failure of fluid-filled cellular solids: theory and experiment, *Proc. Natl. Acad. Sci.*, 2000, **97**(4), 1370–1375.
164. A. Weber, S. Braybrook, M. Huflejt, G. Mosca, A.-L. Routier-Kierzkowska and R. S. Smith, Measuring the mechanical properties of plant cells by combining micro-indentation with osmotic treatments, *J. Exp. Bot.*, 2015, **66**(11), 3229–3241.
165. C. Wei, E. Steudle and M. T. Tyree, Water ascent in plants: do ongoing controversies have a sound basis?, *Trends Plant Sci.*, 1999, **4**(9), 372–375.
166. T. Zhang, H. Tang, D. Vavylonis and D. J. Cosgrove, Disentangling loosening from softening: insights into primary cell wall structure, *Plant J.*, 2019, **100**(6), 1101–1117.
167. Y. Zhang, J. Yu, X. Wang, D. M. Durachko, S. Zhang and D. J. Cosgrove, Molecular insights into the complex mechanics of plant epidermal cell walls, *Science*, 2021, **372**(6543), 706–711.
168. Q. Zhao, X. Yang, C. Ma, D. Chen, H. Bai, T. Li, W. Yang and T. Xie, A bioinspired reversible snapping hydrogel assembly, *Mater. Horiz.*, 2016, **3**(5), 422–428.